2010-07-06

OH Megamasers in Merging Galaxies: A Multi-Frequency Study of IIZw096

Kirstin Marie Cooprider
Brigham Young University - Provo

OH MEGAMASERS IN MERGING GALAXIES:

A MULTI-FREQUENCY STUDY OF IIZW096

by

Kirstin Cooprider

A thesis submitted to the faculty of

Brigham Young University

in partial fulfillment of the requirements for the degree of

Master of Science

Department of Physics and Astronomy

Brigham Young University

August 2010

BRIGHAM YOUNG UNIVERSITY

GRADUATE COMMITTEE APPROVAL

of a thesis submitted by

Kirstin Cooprider

This thesis has been read by each member of the following graduate committee and by majority vote has been found to be satisfactory.

_____   _____
Date   Dr. Victor Migenes, Chair

_____   _____
Date   Dr. J. Ward Moody

_____   _____
Date   Dr. Clark Christensen

BRIGHAM YOUNG UNIVERSITY

As chair of the candidate's graduate committee, I have read the thesis of Kirstin Cooprider in its final form and have found that (1) its format, citations, and bibliographical style are consistent and acceptable and fulfill university and department style requirements; (2) its illustrative materials including figures, tables, and charts are in place; and (3) the final manuscript is satisfactory to the graduate committee and is ready for submission to the university library.

_____   _____
Date   Dr. Victor Migenes
                                 Chair, Graduate Committee

Accepted for the Department

                                 _____
                                 Dr. J. Ward Moody, Graduate Coordinator
                                 Department of Physics and Astronomy

Accepted for the College

                                 _____
                                 Dr. Thomas W. Sederberg, Associate Dean
                                 College of Physical and Mathematical Sciences

ABSTRACT

OH MEGAMASERS IN MERGING GALAXIES:

A MULTI-FREQUENCY STUDY OF IIZW096

Kirstin Cooprider

Department of Physics and Astronomy

Master of Science

OH Megamasers (OHMs) generally appear in luminous infrared regions *i.e.* merging galaxies. In this study we assume that OHMs may not be represented by their association with star formation solely, because of the possibility of a compact AGN source in the merging galaxies. In fact, previously classified starburst galaxies where OHMs are found are now optically observed as AGN. OHMs may also serve as a reasonable criterion for the evolutionary stage of the merger. This project focuses on observations from a multi-frequency analysis of merging regions with known OHMs. Optically, H_α and BVRI filters provided an environmental perspective of the "masing" components. In the radio, 18-cm data was used to determine the structure and position of the OHM. We studied the source IIZw096 and compared our results with two familiar OHM sources. We were able to look at each source at high radio resolutions and compare the structure and classification of each.

ACKNOWLEDGMENTS

Contents

List of Figures

Chapter 1

Introduction

1.1 Project Motivation

Masers (MASER: microwave-amplification-of -stimulated-emission-by-radiation) are interesting because their structures are closely related to the molecular densities of the regions in which they are formed. These molecular regions are found in regions of star formation, interstellar material, and merging galaxies. In these regions masers trace where the density is high enough to induce the amplification of molecules like H_20, OH, Si, and methane.

If the conditions are right, maser emission is helpful in determining the proper motion and physical conditions of the environment of the source. The motion of a maser can show movement in a molecular cloud where star formation is occurring, rotating disks around and Active Galactic Nuclei, and even the expanding shell of an evolving star. In this project OH megamasers (OHM) are used to probe the inner regions of merging galaxies, where star formation and active nuclei may be present.

OHMs appear in luminous infrared regions (merging galaxies) otherwise known as luminous infrared galaxies (LIRGs).[1] Because of the possibility of compact Active Galactic Nuclei (AGN) in the merging galaxies, previous models of OHMs that predict extreme star

1

formation as their only driving mechanism, may be incomplete. Some previously classified starburst galaxies where OHMs are found, are now optically observed as AGNs. Some of the most luminous infrared galaxies seem to have luminosities that correlate more to AGN than to Starbursts.[2]

Because there is a link between OHM and the FIR luminosity, there is also a link between FIR luminosity and molecular gas density. Coupled with this assumption is that late stage mergers show a higher FIR luminosity because merging galaxies are finally beginning to mix and accumulate to higher densities. As the FIR increasing theoretically so do the number of OHMS and as the molecular gas density increases the evolution of a merger continues to a later stage.[1]

Besides the increase of IR radiation due to colliding galaxies, AGN and SBN can contribute to the increase of FIR emission and therefore also increase the number of OHM. They may also be a limited condition for the existence of OHMs and explain why not all LIRGs are OHM sources.

The classification of LIRGs is complicated because of the differing original galaxy types that enter into a merger, some of which may be more starburst dominated while others may contain AGNs. As we look at different mergers we wish to say something about the evolution of the merger based on OHM emission and BVRI and H_α emission.

1.2 Objectives and Problems

All observations in this study are part of a multi-frequency analysis of the merging regions surrounding known OHMs. The $H\alpha$ and BVRI filtered images provide an optical/near IR perspective of the masing components.[3] The radio data refine the positional and structural information of the maser spot. In the end, just as the short wavelength data provide a basis for understanding the properties of the maser components, so do the maser components

constrain the short wavelength image interpretation.

In this project we studied three different merging galaxy regions. Two of the three galaxies, ARP220 and IIIZw035, have been studied extensively, and have been used as comparison sources because they were classified as both AGN and SBN. IIZw096 is the least studied. The two comparison sources were studied using published and archival radio observations. IIZw096 was studied using 2 sets of VLBI radio data and 1 set of BVRI and H_α optical data. The three sources were compared as OHM emission sources. We used optical data to provide a deeper understanding of the morphology of IIZw096.

We obtained radio observations that were taken using the European VLBI and MER-LIN VLBI networks to map the radio continuum and OH spectral structure. The optical observations were taken with the San Pedro Martir (SPM) 1.5 meter telescope in Ensenada, Mexico. From the radio observations we deduced the positional information (position angle, flux density, RA and Dec) of the OHM emission. From the optical observations we could derive the star formation rates.

Statistically improving the study of OHMs in galactic mergers will aid in resolving the debates over classifying LIRGs as AGN and/or Starburst galaxies and explain why OHMs are found in both cases. Also, by determining the classifications more accurately from radio and optical data we can deduce more about the evolutionary stages of mergers.

1.3 Scientific Significance

At least 11 OHMs have been observed at high spatial resolutions, and 90 observed using only a single dish. OHMs are sensitivity limited. While sensitivity can be achieved using large single dish instruments (Arecibo, Green Bank Telescope, etc...), high resolution is necessary and important for understanding the compact components of the OHMs regions. In general these multiple observations will provide a comparison between the physical characteristics

of the OHM emission at a high resolution and the characteristics of the host galaxies. As stated previously, merging systems magnify the star formation process. This is due to the concentration of the molecular gas near the center of the merger. The consequence of this concentration is FIR emissions caused by either starburst dust or AGN, both of which may initiate OHM activity.

Chapter 2

Environment

2.1 Merging Galaxies

The evolutionary steps of a pair of galaxies merge (see Figure 2.1) in approximately the following order:

1. Two gas rich galaxies collide.

2. Large-scale exchanges of angular momentum occur.

3. A significant fraction of the dust and gas settles in the center.

4. High densities and dust opacities occur on a scale of a few hundred parsecs.

5. Bursts of star formation occur inducing hot young stars and supernovae.

6. Ultraviolet luminosity is re-processed by the dust into the far-infrared.

7. Supernovae remnants introduce relativistic electrons to the medium giving rise to synchrotron radio emission.

5

Figure 2.1 Antennae Galaxies. Image found at http://cosmic-web.co.uk/.

The objects involved in the merging process are defined as the Luminous Infrared Galaxies (LIRG). LIRGs are characterized by their high IR luminosities, specifically luminosities that exceed 10^{11} L_{solar}. Ultra-LIRGs (ULIRGs) exceed the FIR luminosity limit of $10^{12} L_{solar}$.

Within LIRGs (ULIRGs), there are compact regions that may contain either Starburst Nuclei (SBN) or Active Galactic Nuclei (AGN). These are known as the possible candidates for a pumping mechanism of maser emission.

2.1.1   Starburst Nuclei

Starburst nuclei are a prime environment for maser emission. The adequate amount of shocked molecular gas provides a good basis for a pumping mechanism. These regions are known for their extreme star formation rates, which exceed that of a normal spiral galaxy such as the Milky Way. These rates are 5.0 M_{solar} $pc^{-2} Gyr^{-1}$ corresponding to 2-

3 stars per year (per galaxy).[4] These intense regions of star formation are dependent on the environmental changes of merging galaxies, shock waves due to rotation, and leftover nuclei due extremely massive stars. The consequences of such events result in explosive star formation and potential maser emission.

There are three factors considered in characterizing starburst galaxies:

1. The rate at which gas is converted into stars, or the star formation rate (SFR).

2. The amount of gas available

3. The comparison between the processing of interstellar material and star formation.

Using these factors, a starburst galaxy can be defined as an object that exhausts its available gas through star formation in less time than the age of the Universe (the Hubble time). When star formation rates are compared to the timescale of galaxy rotation(0.25 Gyr), it is found that in extreme cases, the gas reservoir would be exhausted on the order of one rotational period of a disk galaxy. In starburst galaxies the Star Formation Rate (SFR) is normalized with averaged SFRs, which shows their SFR are above unity.

The basic mechanism for starburst is based on the gas content and irregular perturbations within the galaxy. These types of perturbations may be found in merging galaxies or in disturbed rotation modes which may result from interaction between galaxies rather than actual merging.

As mentioned, starbursts require a certain amount of gas to initiate star formation. Gas is composed of many different chemical elements because of the chemical enrichment from stellar evolution. Generally with large amounts of gas there are relatively more massive stars formed. These young, hot stars ionize the hydrogen rich gas, and create HII regions. Most of these hot, massive stars will end their lives as supernovae, at which point most of the stellar material will be ejected into the environment. The interaction between the ejected material and the interstellar medium initiates maser emission.

Generally speaking there are four types of starburst galaxies. Below is a list of the types and some of their properties (see Figure 2.2). The purpose of this study is to study only those found in ULIRGs and LIRGs.

Starburst Galaxies	Characteristics
BGCs	Blue Compact Galaxies- low mass, low metallicity, dust-free objects. Contain hot, young stars, blue in the optical. Most show signs of recent mergers or interactions
ULIRGs	Ultra Luminous Infrared Galaxies - dusty objects. UV radiation is produced by the obscured star-formation, and is absorbed by the dust and reradiated in the IR. This gives it a reddish appearance.
Wolf-Rayet	Galaxy with a large portion of Wolf-Rayet stars
Baby Boom	Extremely high number of stars are formed, higher than even well-known starburst galaxies.

Figure 2.2 The general characteristics of the four type of starburst galaxies[5]

2.1.2 Active Galactic Nuclei

Active Galactic Nuclei (AGN), are highly active regions at the centers of galaxies. They are known for their bi-polar jets and fast spinning accretions disks. Because of the extreme exchange of energy and outflow of material, they may be an adequate source of high energy photons which may induce maser emission. AGN's different classifications are thought to depend on the line of sight of the observer, the size and density of the surrounding material, although other characteristics probably play are role as well.

An active nuclear region can fuel matter into compact objects. Super-massive black holes that existed in the galaxies before the merger can form into AGN. This may be caused by the merging activity. Unfortunately, AGN may be well hidden at most wavelengths due to the obscuration of dust and gas. As the merger continues the AGN may begin to dissipate the materials of dense gas and dust. The molecular gas will be confined to a torus, and the AGN will in turn become visible. This also depends on the orientation.
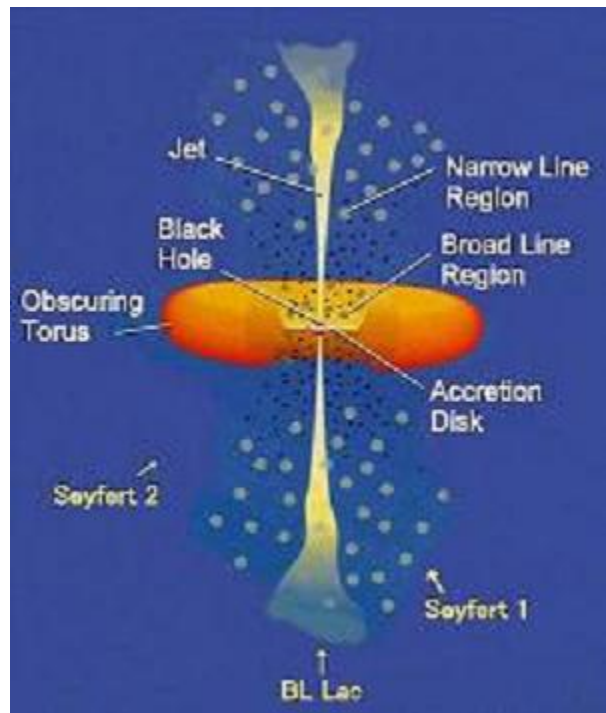
Figure 2.3 Artist's rendition of AGN structure. Image found at http://www.phys.psu.edu/

Radio Quiet AGN	Characteristics
LINER	Low-ionization nuclear emission-line regions, debated if they are true AGN. They constitute the low luminosity class of radio-quiet AGN
Seyfert	Optical nuclear continuum emission, narrow and broad emission lines, strong nuclear X-ray emission, sometimes weak radio-jet emission.
Radio-quiet quasars/QSOs	More luminous versions of Seyferts. Show strong optical continuum emission, X-ray emission, and broad and narrow optical emission lines. Most are found in ellipticals.
Quasars 2s	Quasar like luminosity without stong optical nuclear continuum emission or broad line emission.
Radio-loud AGN	**Characteristics**
Radio-loud quasars	Strong optical continuum emission, broad and narrow emission lines, and strong X-ray emission, together with nuclear, extended radio emission
BLAZARs - (BL Lac & OVV quasars)	Rapidly variable, polarized optical, radio and X-ray emission. BL Lac object show no optical emission lines, broad or narrow.
Radio galaxies	Nuclear and extended radio emission, heterogeneous AGN properties

Figure 2.4 The general characteristic of the various types of AGN[6]

2.1.3 AGN and Starburst Galaxy Classification

As mentioned above, mergers are adequate environments for maser emission because of their concentration of molecular gas. Normally this emission is viewed at 18-cm wavelength due to continuum emission from the starburst or AGN. These observations can distinguish the existence of starbursts and help determine if they really do a play a large role in the existence of OHMs, or if AGN can account for their presence in these systems.

All the OH Megamaser sources we observed appear in a "gray" area between Starburst and AGN defined by photo-ionization models of Kewley et al. (2001), in the diagnostic diagram tool. The BPT diagnostic tool plots the ratio of [OIII]/H_β vs [NII]/H_α (see Figure 2.5). So, while HII regions are ionized by massive stars, AGN ionization originates from a "harder" radiation field. (Baldwin, Phillips & Terlevich (BPT) (1981)[7]). This gray area may indicate an evolutionary transition period.
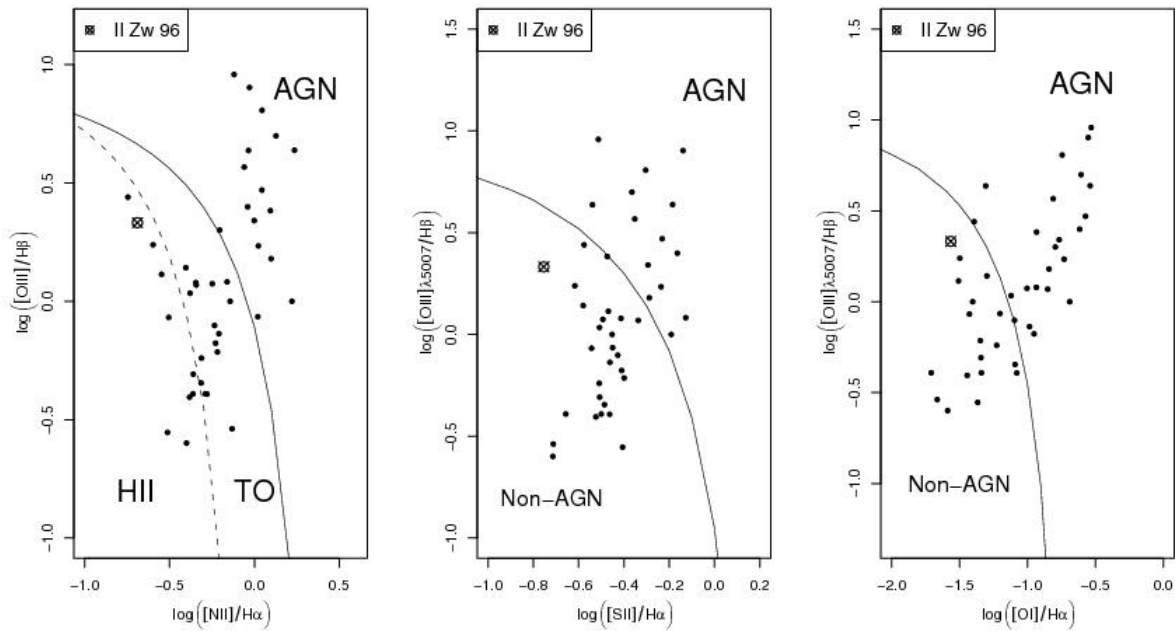
Figure 2.5 Diagnostic diagram used to distinguish between an AGN or SBN(J. M. Islas 2010). The ratios [OIII]/H_β vs [NII/]H_α show a line between commonly accepted AGNs and SBNs. The other plots show similar ratios of [SII] and [OI, which show a comparable relationship to AGN and non-AGN classification. T0 represents potential composite AGN and SBN objects. All of the points on this diagram are OH Megamaser sources taken from the Baan *et al.* optical and radio study (1998).[7] The squared-cross is where IIZw096 falls in this classification. See Appendix B.

Chapter 3

MASER-Microwave Amplification by Stimulated Emission of Radiation

3.1 Basic mechanics

MASERs (Microwave Amplification by Stimulated Emission of Radiation) are akin to the familiar LASERs (Light Amplification by Stimulated Emission of Radiation), and are produced by electronic excitation and subsequent radiatively induced de-excitation as molecules in space absorb and emit microwave radiation. Masers and lasers differ in the wavelength at which the photons are emitted. Shorter wavelength lasers are produced in atomic transitions in contrast to molecular transitions which produce masers. Absorption, a general term for radiative atomic excitation, occurs when molecules interact with photons, being bumped into an unstable, excited state. From there they drop to a lower metastable state. In spontaneous emission the molecule moves to a lower energy state on its own shedding its energy as an emitted photon (radiation).

Stimulated emission differs somewhat from this process. After a drop to a lower, metastable state with a lifetime of about 10^{-3} s, stimulated emission occurs when a photon of the same
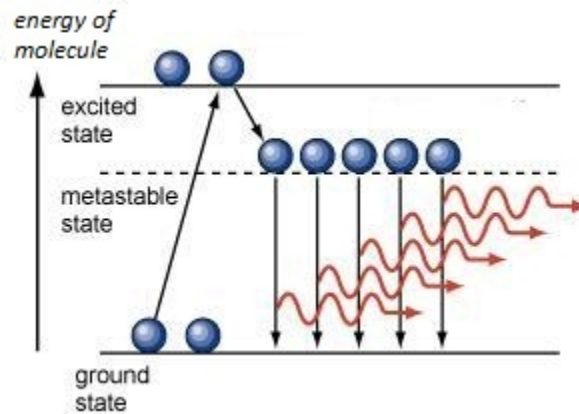
Figure 3.1 A simplicist model of the excitation and amplification of maser emission[8]

energy as the metastably excited molecule interacts with the molecule which then drops to the ground state and emits an identical photon of the same energy as the stimulating photon. It is important to note that the stimulating photon and the stimulated photon must have the same wavelength and phase as the conservation of energy and momentum laws require.[9] Figure 3.1 shows a simplistic model of maser emission.

Below are the 3 principal types of masers which describe the populations of masers found in an astrophysical setting.

1. Stellar masers - found in stellar envelopes of late-stage stars like red giants or red supergiants.

2. Interstellar masers - found in the interstellar medium in regions of recent star formation or in regions of supernova remnants.

3. Megamasers - found in molecular clouds, active galactic nuclei (AGN), or starburst galaxies.

3.2　Population Inversion and Radiative Transfer

To fit all of this information into a mathematical system, first consider the radiative process going on when the microwave radiation is emitted. The radiative transfer equation is a mathematical model that describes how the radiation intensity varies as a function of distance traversed (Equation 3.1). This equation can be modified to describe the brightness temperature variation and helps to understand the fundamental physics with respect to population inversion. Given its intensity, the brightness temperature is the supposed temperature of a non-thermal body, if it were a blackbody in thermal equilibrium.

$$\frac{dI}{dl} = -(\kappa I) + \epsilon \tag{3.1}$$

Equation 3.1 states the change in intensity I over a given length l is equal to the losses (intensity multiplied by the volume absorption coefficient) plus the gains (volume emission coefficient). Both of these coefficients are functions of the populations of the particles moving from the ground state to the excited state, and in the case of maser emission, back to a lower energy state.

$$\kappa = \frac{h\nu}{4\pi\Delta\nu} n_l n_2 B \tag{3.2}$$

$$\epsilon = \frac{h\nu}{4\pi\Delta\nu} n_2 A \tag{3.3}$$

The variables κ, the absorption coefficient (Equation 3.2) and ϵ, the emission coefficient (Equation 3.3) are functions of the Einstein's coefficients (A and B) which are probabilities of the given transitions. Furthermore $\Delta\nu$ which is the Doppler line width, h which is Plank's Constant, n_1 and n_2 which describe the population of the 1st and 2nd energy states and ν which is the line central frequency also describe κ and ϵ.

Population inversion occurs when there are more molecules in the excited state than in the lower energy states putting the system into a state of non-equilibrium. Population inversion itself is a function of the rate at which the population can be redistributed, the pumping rates, and the direction in which the (microwave) photon is emitted. The definition of the population inversion is seen below in Equation 3.4.

$$\Delta n = n_2 - n_1 = (n_2 + n_1)\frac{\Delta R}{R}\frac{\tau}{\tau + \frac{2BI\Omega}{4\pi}} \tag{3.4}$$

R and ΔR are the sum and difference of the pump rates, Ω is the beam solid angle, τ is the rate at which the population can be redistributed, and B is an Einstein coefficient. Equation 3.4 mathematically represents the change in populations from one state to another under population inversion conditions. This equation is closely related to the Saha equation which describes the population distribution in ionization states.[9]

3.3 Stimulated Emission

The next question is what is actually making maser emission possible–what is the input for this simplistic model of molecular excitation and de-excitation? Stimulated emission occurs when a radiative photon induces de-excitation. Stimulating radiation can be from either background radiation (discrete radio sources, SBN, and AGN, see Chapter 3), or spontaneous emission from the boundary of a maser. Maser "pumping" (initial molecular excitation) may also be dependent on these types of radiation. Before discussing the pumping mechanism it is also important to understand what happens to the molecules when they drop to a ground state and how that affects the "masing" process. After the molecules move back to a ground state, they can be re-distributed into the pumping cycle to provide more molecules into an excited state.

In the case when the maser photon emission rate is proportional to the number of

molecules being de-excited, it takes an excitation rate two times the maser photon emission rate in order replenish the population to its original state. In this case the system is said to be saturated. This level of saturation plays a role in the efficiency of the pumping mechanism and the maser emission rate and strength (see Section 3.4). The more saturated the system, the stronger the intensity. For example H_2O masers with an intensity of $10^3 - 10^6$ Jy are probably some of the most saturated H_2O masers seen in the universe.[10]

3.4   Pumping Mechanism

Pumping mechanisms normally fall into two categories, radiative or collisional. There are also chemical reactions that may induce excitation, but these are not normally a significant pumping mechanism in astronomical masers. Both mechanisms are dependent on the molecular and physical properties of the system. This includes the temperature, the density, and the collisional cross-sections. Both mechanisms have limiting conditions. For either the radiative or collisional mechanism there must be at least one collision or radiative absorption for the pumping to occur. More specifically for the radiative model, the pumping radiation must be within the physical region of the maser.[10]

Radiative pumping models are more commonly understood by observations which include the radiation that initiates excitation (SBN and/or AGN). With this in mind the efficiency between input and output can be determined. Generally the pumping rate is proportional to the number of photons absorbed, which is intrinsically linked to the number of photons emitted at microwave wavelengths. This can be demonstrated in terms of luminosity, which is to say that the luminosity of the radiation pump is proportional to the microwave radiation. Careful understanding of the geometry must be considered. The positioning of the pump will determine how many atoms will be excited. If the pump only partially hits a maser region, only some of the atoms will be excited, meaning the pump itself is not being as efficient as

it potentially could be if it were either enveloped in the maser region, or directly positioned to emit all radiation towards the maser region.

In contrast, collisional pumps are never directly observable. Particles, molecules, or atoms that play a part in the collision cannot be detected because they are not radiating. This in turn makes it hard to determine the efficiency of the collision. But in general, by looking at the number of photons emitted or lost due to microwave radiation, the pumping rate should be proportional to the number of photons emitted. The collisional model is less understood because of the lack of observable properties; however, it is not necessarily less common.

Both of these models require a careful understanding of geometry and potentially varying medium conditions. There are cases where the velocity gradient varies throughout the media which may affect the pumping mechanism.[9]

These models are also described by how they function within a specific medium. In the interstellar medium radiative and collisional models are suggested for H_2O masers. Maser emission may occur because of collisions with hydrogen excite the H_2O molecules or because hot dust grains in the medium are radiatively excited by photons. In a paper by Matveyenko,[11] which traced H_2O masers in Orion KL, the technicalities of maser pumping were described as the effect from the central star (or galaxy) and/or an infrared source.

Other masers are believed to be initiated by OH molecules colliding with charged molecules moving along magnetic field lines, but it has also been suggested that OH collisions between molecular hydrogen may create the same sort of emission.[11] SiO masers are pumped by the rotational transitions of the first excited vibrational state of the molecule. Elitzur later proposed a model where SiO could be pumped by a cycle of collisional excitation and radiative de-excitation. This seems to work in regions of high density and close to a stellar surface. Although pumping models have not been solidified, maser emission is still key to much of the scientific progress in understanding the interaction of radiation with material, especially in regions of high density and high energy.[10]

3.5 Maser Geometry

Masers can also be classified by size and shape. Two models are currently developed, cylindrical and spherical though there are also models that describe masers as filaments (see Section 2.6.1). A cylindrical shaped maser is described by its length L, its diameter p, and the beam angle, Ω, as seen in Equation 3.5.

$$\Omega \sim \frac{p}{L^2}. \tag{3.5}$$

Cylindrical symmetry has a preferential line of emission. If the cylindrically shaped maser's axis is not pointed along the line of sight its maser emission will not be observed. In contrast, the spherically shaped masers are described by a diameter and a beaming angle proportional to $1/D$ which means that the observer only sees emissions along the lines that pass through the center of the sphere.

Other variables to consider are the line width (depends on the molecules being excited), the saturation, and the polarization (normally either linear or circular). In a study by Knowles and Batchelor 25 % of the H_2O masers detected had polarized features. Polarized features have also been found in SiO masers (primarily found around stars) and even in OH regions.[12] Polarization could indicate properties of the magnetic field in the region of emission.

3.6 OH Megamasers

Because of their existence in merging galaxy environments this thesis includes only observations of OH megamasers. While OHMs are normally observed in regions of active stellar formation, we propose that AGNs also supply a possible pumping mechanism. These masers were first found in the peculiar galaxy ARP220. Unlike normal galactic OH masers, their emission was a factor of 10^6 times bigger. See Figure 3.2 for the hyperfine structure of an

OH maser which includes the transitions of OH megamasers. The velocity width was on the order of a few hundred km/s, and the emission was dominantly found in the 1667 MHz line. Although there are OH emission lines at 1667, 1665, and 1720 MHz, their complex line profiles may be connected to the polarization and the rotation of the galaxy. As mentioned, OHMs are connected to FIR galaxies, ultra-luminous infrared galaxies, and those exceeding luminosities of 10^{12} L_{solar}. But not all ULIRGs show OHM emission, and the detection seems to be a function of the FIR luminosity. As FIR luminosity increases, so do the detection rates of the OHMs. There has been evidence that there are multiple velocity components, weaker and stronger, with velocity widths up to 1000 km/s.[13]
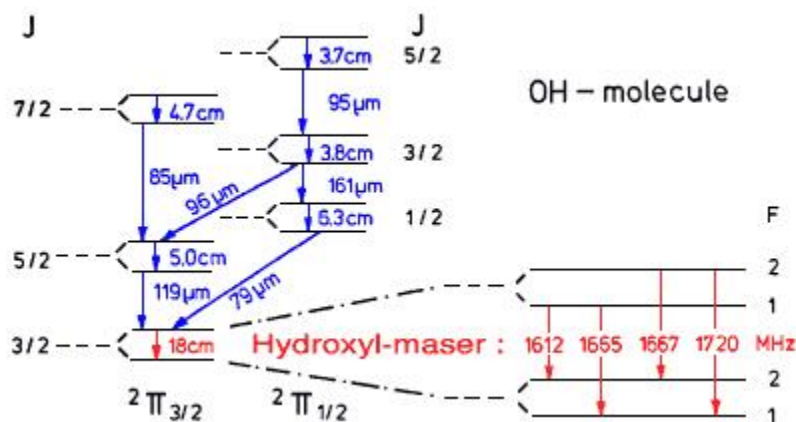
Figure 3.2 The hyperfine structure of OH, showing the 4 possible transitions at 1612, 1665, 1667, and 1720 MHz[14] OH Megamasers only seem to exhibit 1665 and 1667 MHz transitions.

The 18-cm spectral lines for OH were the first detected by radio astronomy techniques. These lines are formed in small bright patches, as small as diameters of 0.1 arcseconds and at brightness temperatures near 10^{12} K.[15]

3.6.1 OHM geometry theories

Differing theories discuss the difference between diffuse and compact maser emission. As the pumping mechanism is disputed, so are the structural components of OHMs.

Diffuse OHM sources at scales greater than 0.1 arcsec, where OHM are found in the rotating disk or tori, are found to arise from FIR radiative pumping due to energetic photons from AGN or starburst activity deeper within the nuclear regions. Compact OHM emission may require certain associated properties including the necessity of a compact object embedded in a diffuse region, namely an AGN. For us to see all of the maser emission and for the maser to attain fullest efficiency, all masers must be in our line of sight and the maser must be in line with the stimulating photons. Some factors that determine the directional efficiency of the emission are the size of the maser, the velocity field, and filamentary shape.

Three theories describe the shape and compactness of OH masers. If the maser is relatively small it will appear to radiate isotropically (like a point source), though this does seem to be problematic with other IR pumping schemes. There is also the possibility that the velocity field is anisotropic, so that the velocity is only in one direction. While this is probable, there is no mechanism to explain it sufficiently. Turbulence of the medium might also affect the directionality of the velocity. Lastly, maser spots may take the shape of filaments with high velocity dispersion. The compactness is dependent on the filament straightness and transverse diameter, not totally on the direction of the filament.[13]

These properties imply a few other characteristics of the medium. The first implies the existence of a compact IR source, such as a dusty torus around an AGN or a SBN. The second may have to include both radiative and collisional pumping models to induce the correct amount of excitation in the masing region, and increase the probability of hitting the cloud. The third, implying filaments, must include constraints on the diameters of the filaments and the internal velocity. These types of limitations may help to bridge between diffuse and compact models of OH Megamasers.

The most likely explanation of compact masers is a combination between the first, small masers, and the third, filamentary geometry. An elongated, compact cloud buried in the innermost dense regions of sources with high FIR opacities, is capable of producing the

observed maser structures by radiative pumping alone.[13]

Although we do not focus on polarization and variability in this project, they are still properties worth mentioning. Polarization may help us to unravel the occurring Zeeman effect processes and the presence of magnetic fields. In terms of variability, OHMs change on timescales of years in contrast to H_2O masers that may vary in days and months. Variability seldom masks identity and therefore still allows for proper motion studies.

Chapter 4

Optical and Radio Astronomy

4.1 BVRI and H_α

Optical data pinpoints the greatest probability for regions of star formation. Visible H_α and neutral hydrogen intensities correlate well with such regions. H_α is emitted as part of the process of the recombination and de-excitation of electrons and protons in a warm ionized medium. Its rest-frame wavelength is 6563 $\mathring{A}$. The emission is from recombination after photo-ionization by UV photons associated with regions of massive star formation. By determining the H_α emission rate, one can analyze and determine the star formation rates (SFR).

Star formation rates can be determined and related to the system from the H_α calibrated fluxes. The star formation rates found for our galaxies were derived using the Salpeter initial mass function (IMF) with stellar masses between 0.1 and 100 solar masses.[3]

B,V,R and I filters are also useful for population identification. When an image is redder the associated population is older or has higher metallicity in contrast to younger, bluer populations of lower metallicity. The population type and the star formation rate tell something about the system and how the galaxy merger is evolving. As this is not the main focus of

the project, we do not include an in depth description of the science. See Coziol *et al.* (2004) for more information.[16]

We used the San Pedro Martir 1.5, which included filtering capabilities necessary for radio/optical comparison studies.

4.1.1   San Pedro Mártir 1.5 meter telescope

The San Pedro Martir (see Figure 4.1) observatory is operated by the National Astronomical Observatory of México. It was built in the late 1960s for the higher quality skies in its remote location. Since the late 1970s the telescopes have been used for research purposes. Research projects include variables stars, stellar chemical abundances and ages, and spectroscopy. Currently there are three telescopes at the San Pedro Martir observatory outfitted with CCD detectors, UBVRI photometers, a photographic spectrograph, photographic and CCD cameras, a fast double-photometer, and an optical interferometer.[17]

Figure 4.1 An image of the San Pedro Martir facilities in Ensenada Mexico[18]

4.2 Radio Astronomy

In 1935 Karl Jansky, of Bell Labs, used his dipole radio antenna (see Figure 4.2) to detect something new: a signal that could only be explained by radio emission from the Milky Way. From this discovery came a new facet of astronomy, one that would depict the universe in another perspective. Radio astronomy gives us information about many sources that cannot be seen in the visible simply because of dust obscuration as well as some sources that do not emit visible radiation. Radio astronomy can probe the inner regions of star formation and the inner depths of the Galaxy, map regions of hydrogen, using the 21-cm line, and can be used to study the distribution of molecular gas.
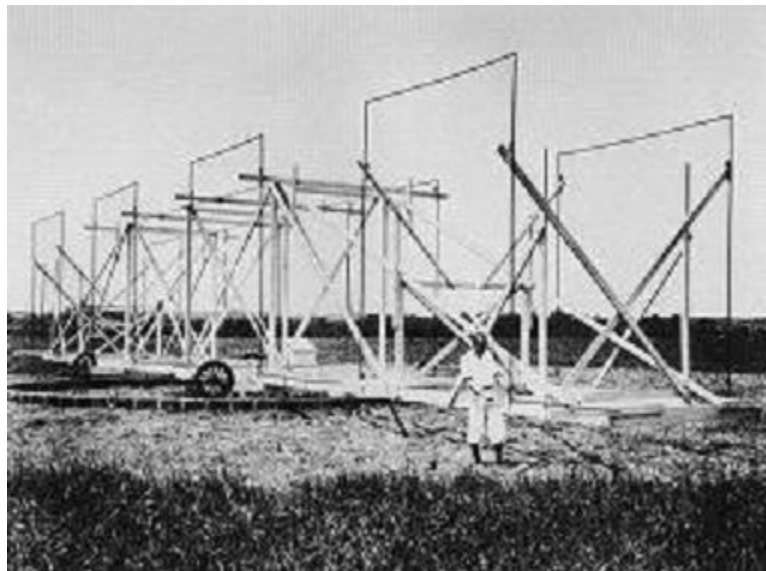
Figure 4.2 Jansky's first dipole antenna[19]

In this chapter we will describe the fundamental physics behind radio astronomy, including interferometry and some of its common observational techniques and instruments.

4.2.1   Fundamentals

The resolution of a telescope is given by Equation 4.1 where θ = angular resolution, λ = wavelength and D = aperture size. Because radio wavelengths are larger aperture size (baseline) must be larger to attain a comparable resolution.

$$\theta \approx \frac{\lambda}{D} \tag{4.1}$$

For example, the Hubble Space telescope has an aperture of 2.4 meters, and has a resolution of 0.04" for a wavelength of 5000 Å. If in the radio spectral region we want the same resolution for something at a wavelength of 18 cm, we would need a telescope 864 km in diameter!

4.2.2   Interferometry

To overcome this seemingly impossible construction, instruments to observe radio sources are based upon the technology of interferometry. Interferometry allows a researcher to observe at much higher resolutions than attainable by even the largest single-dish radio telescopes. The larger the baseline the greater the resolution. As is expected, radio waves require larger apertures to reach the resolution of common optical telescopes.

Interferometry gathers the data of several antennas and mathematically combines the data using correlators and fast fourier transforms (FFT). It is in the correlator that the sampled voltage time series of two or more antennas are combined, to produce sets of complex visibilities, V_{ij}. The visibilities are a function of frequency, antenna pair and time. They are the data points used for imaging and spectroscopy.

Because synthesis arrays can be analyzed by looking at combinations of two-element arrays, we will discuss the properties of a two-element instrument (see Figure 4.3).

From Figure 4.3 we see a simple block diagram of a two-element array. The two antennas
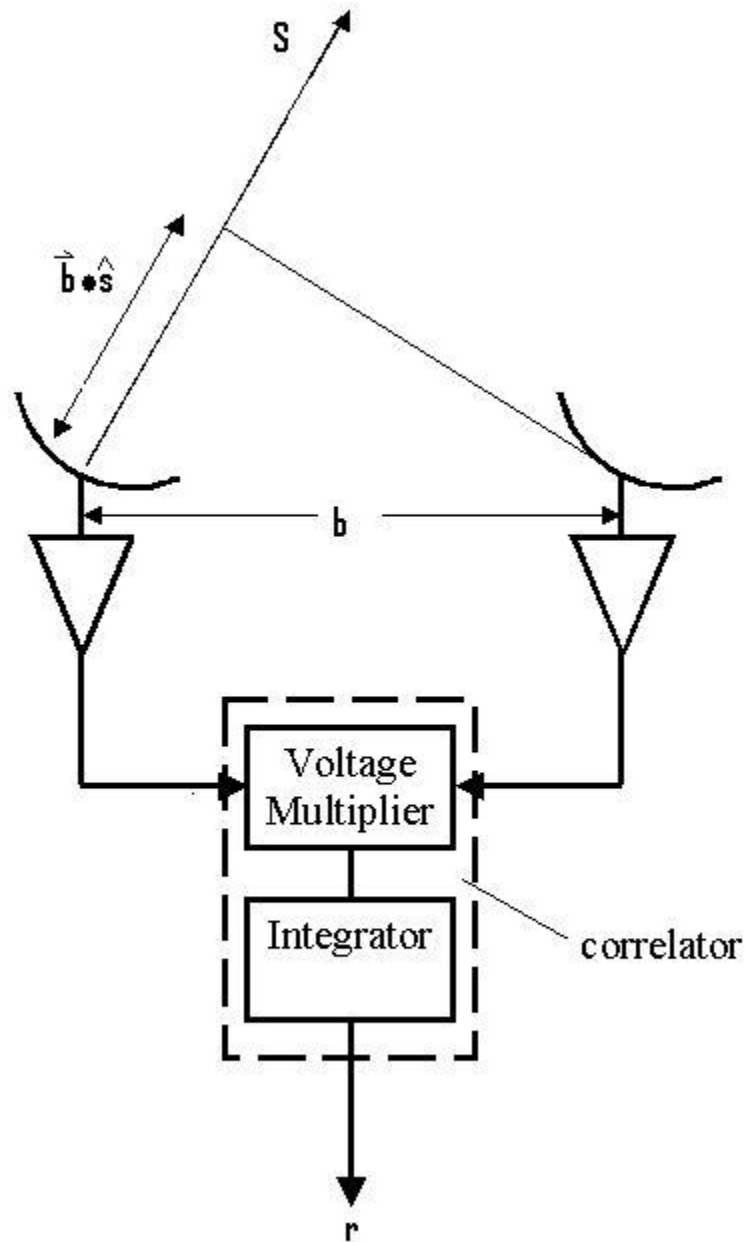
Figure 4.3 Schematic diagram of 2 interferometric antennas[20]

point towards a radio source in the direction of the unit vector $\hat{s}$. The interferometer baseline is **b** which is a vector from antenna 1 to antenna 2. The time delay it takes the wavefront to reach the second antenna after reaching the first is τ_g. This is also called the geometric delay which is given by

$$\tau_g = \vec{b} \bullet \hat{s}/c \tag{4.2}$$

where c is the speed of light. The signals from the antennas pass through amplifiers, which contain filters to select the required frequency band width $\Delta\nu$ centered on the frequency ν. The signals are combined in the correlator, which is a voltage multiplier followed by a time-averaging circuit.

The output from the correlator is

$$r(t_g) = v_1 v_2 \cos 2\pi\nu\tau_g \tag{4.3}$$

where t_g is the phase, and v_1 and v_2 represent the fringe amplitudes which are proportional to the received power for the respective antennas. The cosine terms represent the motion of the source through the interferometer fringe pattern. In the end we want the signal (starting as a voltage) in terms of intensity or radio brightness integrated over the sky.

As a small segment of the signal dr leaves the correlator it can be represented by the solid angle $(d\Omega)$.

$$dr = A(s)I(s)\Delta\nu d\Omega \cos 2\pi\nu\tau_g \tag{4.4}$$

A(s) is the effective collecting area in the direction of s and I($\hat{s}$) represents the radio brightness in the direction of the unit vector $\hat{s}$ at a frequency ν. The value dr can be integrated to give us the final signal over the celestial surface which subtends 4π steradians. The beam width of the antenna, the finite dimensions of the radio source and other restrictions on the field of view will make the integrand fall to low values outside a small angular field.

r can be represented in terms of baseline and source position:

$$r = \Delta\nu \int A(s)I(s) cos\frac{2\pi\nu\vec{b} \bullet \hat{s}}{c} d\Omega \tag{4.5}$$

We assume the bandwidth is sufficiently small that variation of A and I with ν can be ignored. We also assume that the source must be in the far field of the interferometer so that incoming wavefronts can be considered to be plane to the telescope. And we assume that different points from the source can be added independently.

For observations to make an interferometric image we may choose somewhere to center our synthesized field of view. This is important, especially with a very weak source, because then the phase can be calculated with respect to the phase reference position. This is known as $\hat{s_o}$. $\hat{s}$ is the target position vector and $\vec{\sigma}$ is the angle between $\hat{s_o}$ and $\hat{s}$ (see Equation 4.6).

$$\hat{s} = \hat{s_0} + \vec{\sigma} \tag{4.6}$$

now r can be described in terms of the phase reference position.

$$r = \Delta\nu \cos\left(\frac{2\pi\nu\vec{b}\cdot\vec{s_o}}{c}\right) \int_s A(\vec{\sigma})I(\vec{\sigma})\cos\left(\frac{2\pi\nu\vec{b}\cdot\vec{\sigma}}{c}\right)d\Omega \tag{4.7}$$

$$-\Delta\nu \sin\left(\frac{2\pi\nu\vec{b}\cdot\vec{s_o}}{c}\right) \int_s A(\vec{\sigma})I(\vec{\sigma})\sin\left(\frac{2\pi\nu\vec{b}\cdot\vec{\sigma}}{c}\right)d\Omega$$

Lastly we introduce the idea of visibility which is a measure of coherence. More specifically it is described as an un-normalized measure of the coherence of the electric field, somewhat altered by the characteristics of the interferometer. The complex visibility of a source is defined as:

$$V(u,v) = |V|e^{i\phi v} = \int_s \vec{A}(\vec{\sigma})I(\vec{\sigma})e^{-2\pi i\nu\vec{b}\cdot\frac{\vec{\sigma}}{c}}d\Omega \tag{4.8}$$

where $\vec{A}(\vec{\sigma}) = A(\vec{\sigma})/A_0$ is the normalized antenna reception pattern, A_o being the response at the beam center.

$\vec{A}(\vec{\sigma})I(\vec{\sigma})$ is the system's response to the brightness distribution as the antennas are tracking the source.

If we separate the real and imaginary parts we have:

$$A_0|V|\cos\phi v = \int_s A(\vec{\sigma})I(\vec{\sigma})\cos\left(\frac{2\pi\nu\vec{b}\cdot\vec{\sigma}}{c}\right)d\Omega \tag{4.9}$$

$$A_0|V|\sin\phi v = \int_s A(\vec{\sigma})I(\vec{\sigma})\sin\left(\frac{2\pi\nu\vec{b}\cdot\vec{\sigma}}{c}\right)d\Omega \tag{4.10}$$

By substituting 4.8 and 4.9 into equation 4.7 we are left with the following equation of r:

$$r = A_0\Delta\nu|V|\cos\left(\frac{2\pi\nu\vec{b}\cdot\vec{s_o}}{c} - \phi v\right) \tag{4.11}$$

From Equation 4.11 the amplitude and phase of the fringe pattern can be determined, measured by the cosine term. Then the amplitude and phase of V can be derived by proper calibration.[20]

From a two-element array we retrieve one visibility in the $u-v$ plane. Using the separation of two-element array, u is the eastern projection of the separation, and v is the northern projection. If we know V across the entire $u-v$ plane, we can use an inverse Fourier transform of equation 3.6 and find the image through $I(\vec{\sigma})$. In general interferometers are made up of n elements which give us $N(N-1)/2$ visibilities (as a function of time) for each observation.[21] To describe the system visibly, the visibilities can be mapped by false color against the $u-v$ plane.

4.2.3 Very Long Baseline Interferometry

To attain the best possible resolution, very large baselines are required. With such baselines, we can resolve objects outside our galaxy at separations of 10^{18} cm (0.3pc). These interferometers are called very long baseline interferometers (VLBI).

Figure 4.4 The Very Large Array (VLA) near Socorro, New Mexico, is an example of interferometry. The 27 dishes are arranged in a "y"-shape in conjugation with the rotation of the earth to create what can be thought of as one very large radio telescope.[22]

The greatest difference between the VLBI and those such as the Very Large Array (see Figure 4.4) are that they are not connected, and so phase differences cannot be recorded in real time. To accommodate this difficulty, atomic clocks are used to synchronize each telescope in the array. Other problems include: atmospheric differences at each antenna, the curvature of the earth, and the type of telescope at each location. This is an issue especially with an instrument that contain antennas of different size and construction. Because of these complications calibration and antenna weighting is extremely important. In this project we use observational data from the European VLBI Network (EVN) and the Multi-Element-Radio-Linked-Interferometer-Network (MERLIN).

EVN and MERLIN

The EVN is a collaboration of several telescopes across Europe and even to the far regions of Asia (see Figure 4.5). The telescopes are not all the same size ranging from 100 meters down to 10 meters. There are a total of 18 individual antennae, some of which are currently under construction with baselines reaching as far as 12000 km. The EVN observes for 3 periods per year, each session is approximately 3-4 weeks long and involves 3-4 different observing frequencies. It can attain a resolution of about 5 milliarcseconds (18-cm wavelength). Table 4.1 describes some general characteristics of the most frequently used antennas in the EVN array.

The MERLIN array is operated by the Jodrell Bank Observatory, of the University of Manchester (see Figure 4.6 and Table 4.2). The 8 telescopes are arranged within Great Britain with baseline lengths up to 217 km. It operates at frequencies between 151 MHz to 24 GHz. It resolution is better than 50 milliarcseconds.
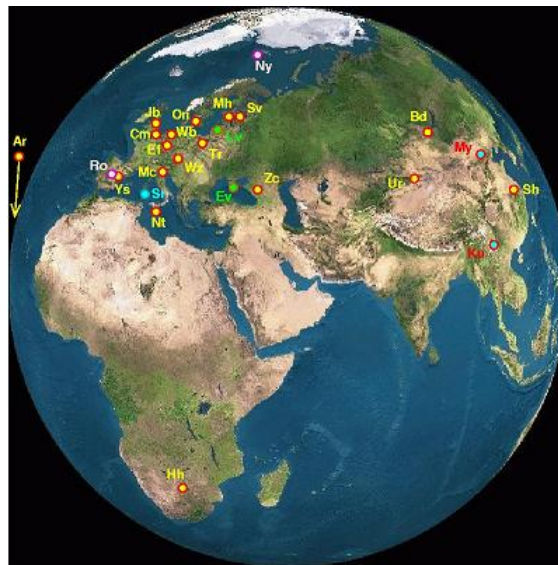
Figure 4.5 The EVN spans across and beyond the European landscape. It is maintained by the JIVE organization in Dwingeloo, the Netherlands.[23]

Name	*Country*	*Size(m)*
Effelsburg	Germany	100
Westerbork	Netherlands	Array Nx25
Cambridge	UK	32
Jodrell Bank	UK	76
Medicina	Italy	32
Shanghai	China	25
Noto	Italy	32
Turon	Poland	32
Onsala	Sweden	25

Table 4.1 The most frequently used elements of the EVN array

Name	*Size(m)*
Lovell	76
Mark II	25
Knockin	25
Cambridge	32
Defford	25
Knockin	25
Darnhall	25
Pickmere(Tabley)	32

Table 4.2 Elements of the MERLIN array
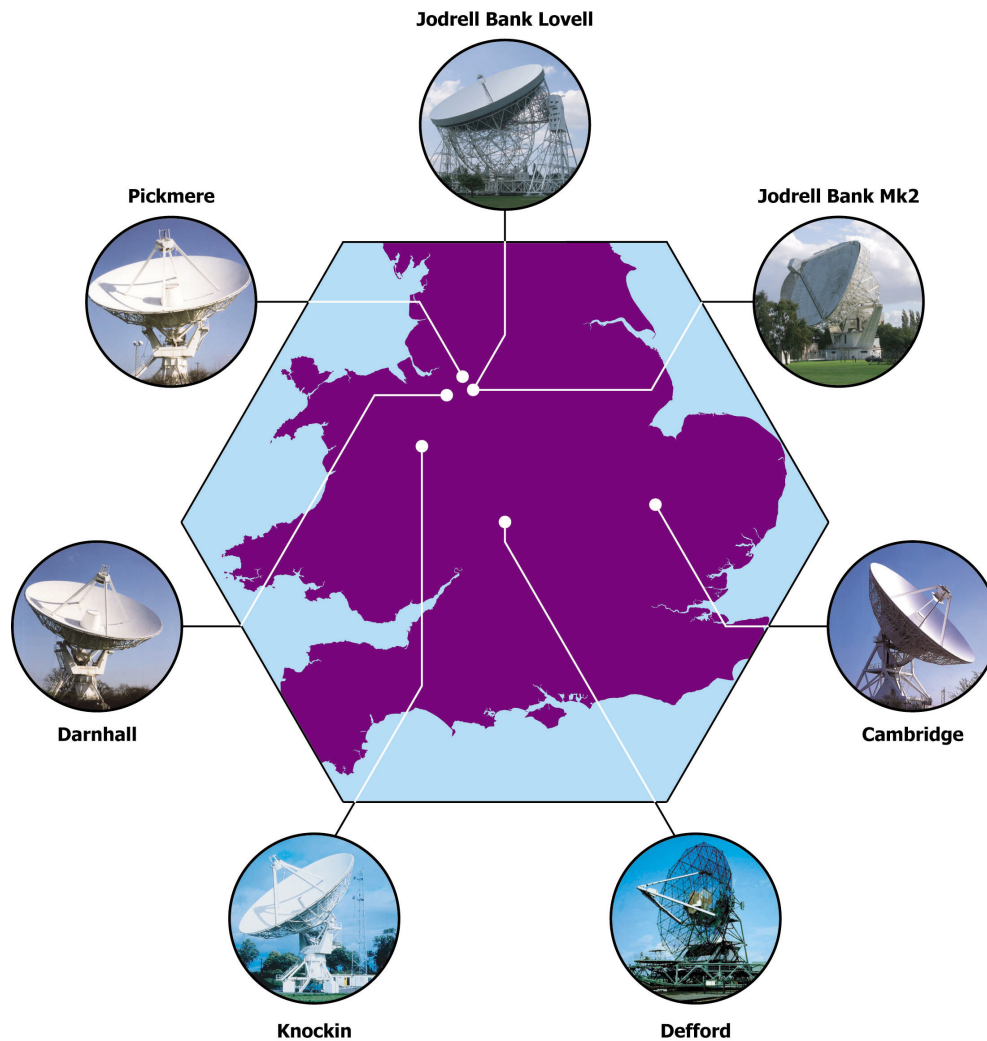
Figure 4.6 The MERLIN array spanning the English landscape. It is similar to the EVN because there are a number of differing sizes and types of telescopes.[24]

4.2.4   Phase Referencing

Because we are using VLBI, phase referencing is helpful for detecting target sources that are too weak to get detectable fringes within the coherence integration time. To overcome this disadvantage, the target source must be calibrated against a another source. This "calibrator" must be strong enough (on the order of a few hundred mJy) to be detected, show no structure, and be within 6 degrees of the target source. Once the phase of the calibrator is determined it is then transferred to the target source, however the model phase must change

slowly over time. This requires constant monitoring of the calibrator and target source. The time between calibrator and target source should be 15 to 30 seconds at 43 GHz and 2 to 3 minutes at 8.4 GHz. The atmosphere, including the ionosphere and troposphere vary with location, thus changing the phase. This must be taken into consideration, especially in the data reduction stage.[25]

Chapter 5

Procedures and Methods

IIZw096 was chosen from the Darlin and Giovanelli 2002 database of OHM sources. We used 18-cm radio data from both the MERLIN and EVN interferometric arrays. We also used optical data ($H\alpha$ and BVRI filters) taken by the San Pedro Martir 1.5 meter telescope. In the optical and IR these ULIRGs show very complicated morphology.

We compared our results with data and publications of IIIZw035 and ARP220. We used the study by Pihlstrom *et al.*[26] of IIIZw035 which used the EVN and MERLIN systems, and Lonsdale's (1998) study of ARP220 which used the EVN array. To supplement and accurately confirm the ARP220 studies, we also looked at some more recent data taken in 2004 with Diamond *et al.* as the primary investigators. All data sets had similar EVN and MERLIN setups.

Source	R.A.	DEC.	Date of Observation	Observing Run(hours)
ARP220	15:35:57.12	+23:30:11.5	Nov 1994 & June[27] 2006	4 & 16
IIIZw035	01:44:30.5	+17:06:05	June 1998[26]	12
IIZw096	20:57:23.3	+17:07:34	July 2004	8

We will describe the observations and the process of data reduction for both the optical

and radio studies although this project is focused mostly on the radio analysis.

5.1 Optical Observations

The BVRI and H$_\alpha$ filtered images were obtained during an observing run of 2 nights in July 2004 on the 1.5-meter telescope from the National Observatory of México, located in the Sierra San Pedro Mártir (SPM), in Baja California. The detector used was a SITe1 CCD with 1024×1024 pixels. The plate scale of the telescope (with focal ratio f/13.5) and camera setting is 9.8 arsec/mm, which, considering a pixel size of 24μm, corresponds to a spatial scale of 0.26 arcsec/pix and yields a field of view of 4.4×4.4 arcmin.

Standard BVRI Johnson filters were used. Three images in each filter were obtained, with respective exposure times of 900 seconds for B, 600 seconds for V and 200 seconds for R and I. Two narrow-band images were also obtained using the filters $\lambda 6819 \mathring{A}$ for the H$_\alpha$ line and $\lambda 6690 \mathring{A}$ for the underlying continuum located to the blue of the line. For each filter, 3 images of 900 seconds were obtained.[3]

5.1.1 IRAF - Imaging Reduction and Analysis Facility

Usual image reduction processes were applied using IRAF. Bias subtraction and median normalized sky flat-fields for each filter were subtracted.

Each bias frame or zero-second exposure was taken with the shutter closed. Several bias frames were taken and averaged. After they were averaged they were put into one master bias frame, and then were subtracted from the flat field frames by using the IRAF command **CCDPROC**.

The flat field frames provide a measure of each pixels' response to light. A flat frame is taken as the charge coupled device (CCD) is exposed to light of uniform intensity to see how each pixel responds. The mean brightness was measured and averaged so that it could

be used to scale the flat frame. The image frames were then divided by the scaled flat. The commands **FLATCOMBINE** and **CCDPROC** were used to make a master flat and then were applied to the image frames.

The individual images were then corrected for cosmic rays and bad pixels using the command **COSMICRAYS**, and combined using the option "average" in **IMCOMBINE**.

IMCOMBINE took a set of images or the planes of an image cube and combined them by using a weighted median average. Bad pixels were rejected by placing pixel masks to the data.

For the BVRI images, the contribution from the sky was determined by measuring the mean level count in several regions around the target, which was subtracted from the images. The final H_α image was obtained by subtracting the corresponding continuum image.

During the run, 24 photometric standard stars from the list of Landolt (1992) and 6 spectroscopic standard stars from the list of Oke (1990) were observed to correct for the telescope and CCD response and calibrate the data in fluxes. All observations were done under photometric conditions.

BVRI calibrations equation were calculated by fitting linear regressions on the observations. Airmass corrections were applied using the extinction coefficients appropriate for San Pedro Mártir (Schuster & Parrao 2001[28]). After transforming the instrumental magnitudes to the standard system, and adopting the best-fit coefficients, the formal errors are: 0.08, 0.09, 0.03 and 0.06 in B, V, R, and I, respectively. The equations for calibrating the surface brightness and color profiles of different zones in IIZw96 were obtained by taking into account the galactic extinction toward this part of the sky.

Flux calibration in H_α was done by fitting a linear curve on the data by observing 3 standard stars: BD +25D4655, BD +28D4211 and GD 248. For each band, the integrated flux was estimated by multiplying the flux density from calibrated spectrum at the center of the band, by the bandwidth. The 95% confidence interval on the slope suggests an

uncertainty of the order of 6% in the fluxes reported in section 6.3.1.

5.2 Radio Observations

We based our radio analysis on two data sets, which could be combined for better u-v coverage. The MERLIN-EVN observations were taken the June 8, 2005. All the telescopes were available at the time of the observations. Observations were done in a phase-referencing mode and spanning 8 hours. Assuming the object had a redshift $z = 0.036$, the channels were centered at 1608.07 MHz (1667.359 MHZ in rest frame). This central frequency offset was used to include both, the 1665 and 1667 MHz frequency transitions. A bandwidth of 8 MHz for both the left and right hand polarization was used to cover the complete velocity range (~ 1000 km s^{-1}).

The EVN data taken in conjugation with MERLIN data was 18-cm data spanning 9 hours with 5 hours on the target source. This data had a similar setup with better spectral and spatial resolution, with the band split up in 256 channels. This set of observations included the Arecibo telescope (305 meter diameter) in Puerto Rico and the Hartbeesthoek telescope (26 meter diameter) in South Africa. The Arecibo telescope did not contribute to the observations until about half way through the 9 hour observing run.

The Arecibo and Hartbeesthoek telescopes were included in these observation runs to increase resolution by introducing larger baselines, and to increase sensitivity with their greater collecting area. The MERLIN and EVN data sets were combined to attain a better determination of the structure of the OHM emission.

The reduction was done using Astronomical Imaging Processing System (AIPS), following the standard procedure. The data set was amplitude-calibrated using the system temperature measurements. Because the low signal to noise ratio (S/N) for weak maser features prevented self-calibration on any individual maser peak, fringe fitting was performed on the

phase reference sources. The data were imaged using robust weighting, with a beam size of 0.2×0.1 mas (where 0.1 mas =0.070 pc at the distance of the object, using $H_0 = 75$ km s^{-1} Mpc^{-1}).[3]

5.2.1 AIPS - Radio Data Reduction

The Astronomy Interferometric Processing System (AIPS) is the method for reducing most radio data. The VLBI network uses this software package for VLBA, EVN, and other interferometric arrays. It is updated and revised continually by the National Radio Astronomy Observatory, and is based in Socorro, New Mexico.

The general format of the AIPS system made up of verbs, adverbs and tasks. Tasks run the basic operations that produce tables and images from the original data set. Verbs and adverbs display and map images and plots from the tables. Generally speaking, the data uploaded into AIPS is never changed. The tables that are produced are the outcome of calibration and reduction.

Our data reduction followed a general recipe of steps from the AIPS Cookbook[29] or in the case of this process from the EVN reduction manual.[30] In the first step we downloaded the data from the archive. This data was in FITS format.

We used FITLD to upload the data into AIPS, making sure to concatenate all of our data. Once our data was uploaded into AIPS it was found in the u-v catalogue, where it was analyzed in POSSM (see Figure 5.1). We looked at the u-v coverage, the amplitude over time and space, and the spectral emission over frequency or velocity. POSSM allowed us to check the data for large errors. We also used UVPLT to look at the data and inspect the "goodness" of the observations, in time and in u-v space. After looking at the data, ANTAB was used to load all of the calibration information including the system temperature information and gain curves.

Once we downloaded the calibration and made other corrections, the data was flagged,
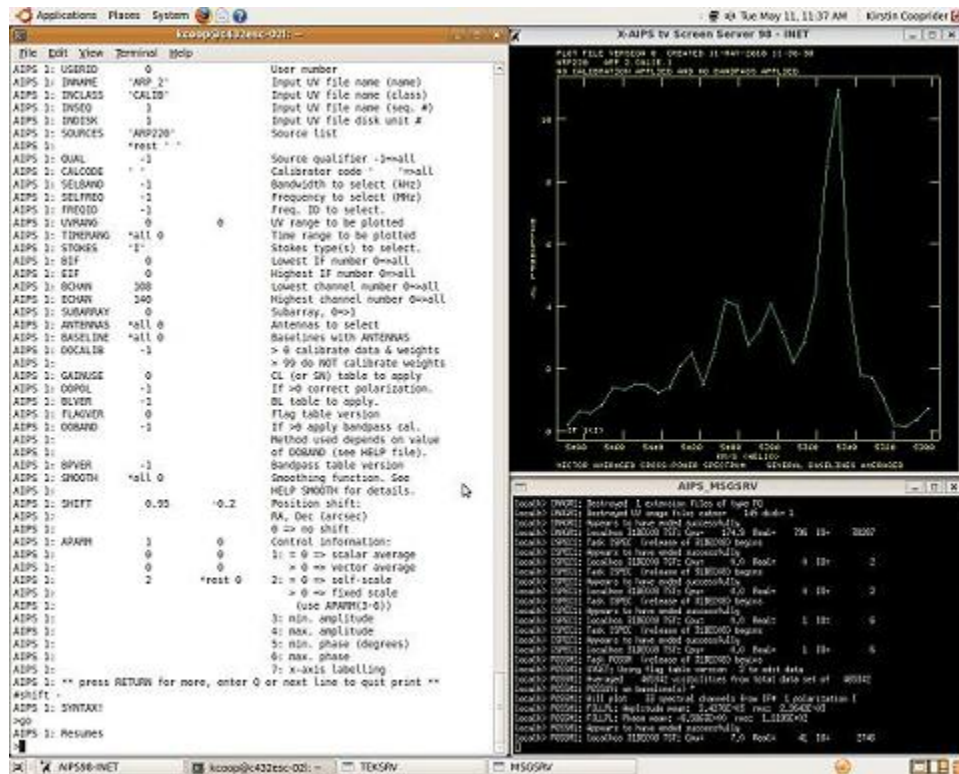
Figure 5.1 The general terminal layout for AIPS program. Includes AIPS terminal, AIPS message server, AIPS tek server, and AIPS TV screen.

to take out bad data points. The tasks most commonly used to flag data are TVFLG and IBLED. There are interactive displays of the data with cutting and flagging capabilities. We created FG tables as a result of our flagging.

Our calibration followed two basic steps: amplitude calibration and phase calibration. For most VLBI data APCAL is used to apply the gain curve information to the data. For the EVN data we used ANTAB. With ANTAB we applied the system temperature and gain-curve information to our u-v data.

It should also be noted that currently many facilities run data through a pipeline to attain preliminary images. This is usually only applied to the continuum; however, it is a good check for amplitude and phase calibration. We used the pipeline tables as a way to check the spectral line data for emission.

After amplitude calibration we applied bandpass calibration by creating BP tables to correct the band over each antenna. Bandpass calibration can be applied before or after phase calibration. In this project we applied bandpass calibration after amplitude and before phase calibration.

We applied the calibration to tables used in the imaging process with the tasks SETJY and CLCAL. These tasks wrote the data to CL or calibration tables. We changed the headers of the files so that the data could be displayed in an alternate coordinate system such as velocity using ALTDEF.

Our last step before imaging was phase calibration, which essentially allowed all the data to be averaged together. With pipeline data it is simply another CL table that has already been made. However, we also went through the process using the task FRING. This process retrieved the phase derivatives with respect to frequency and time, solved them, and then removed them from the data.

After all of the calibration was applied, we adjusted all antennas to a reference velocity and frequency using CVEL. Once the data were correctly shifted, we used SPLIT and SPLAT to split the target source out of the entire multi-source data set.

Lastly that split data were imaged, using the task IMAGR. It made a 3-D cube, Right Ascension (α), Declination (δ) and channel (ν). From these maps, self-calibration was applied to the data to remove or reduce sidelobes in the data (*i.e.* noise). This involved running the data tables through a task called CALIB, or SCMAP. It applied all the tables and maps to itself, to self-correct any errors. A final "clean" map was produced and is used for analysis.

AIPS has a few tasks helpful for analysis. To find mean intensities and fit a gaussian to the maser spot we used the tasks JMFIT and IMEAN. From these tasks we determined the maximum intensities with errors included, as well as position angle, α, δ and RMS. To understand the structural significance of the maser spot we used KNTR to map a contour plot showing the intensity gradient and elongation properties (AIPS cookbook and EVN

analysis guide). We compared all our archival results with the new data and with the two comparison sources to understand more accurately the structure and intensities of the maser spot. Figure 5.3 gives a summary of the EVN reduction process. This process is similar to most VLBI reduction recipes.

MERLIN+EVN

To increase the uv coverage we combined the MERLIN and EVN data using DBCON and UVMOD (see Figure 5.2). DBCON treated MERLIN as another antenna in the EVN array. This required that we average the channels in the EVN data, such that they had the same channel width. Once we had the same channel width we adjusted the amplitude from each array using UVMOD. Because the MERLIN array has better sensitivity because of its uv-coverage, it shows higher flux amplitudes than the EVN, which has better resolution, but lower uv-coverage (hence lower sensitivity). To correct the amplitude difference we found the difference between the two and created a factor in UVPLT. Then we used UVMOD to increase the amplitude factor of the EVN by approximately two. Once we had the correct amplitude scale we combined both data sets using DBCON to form one data set. Self-calibration and data analysis techniques could then be applied to the combined data.
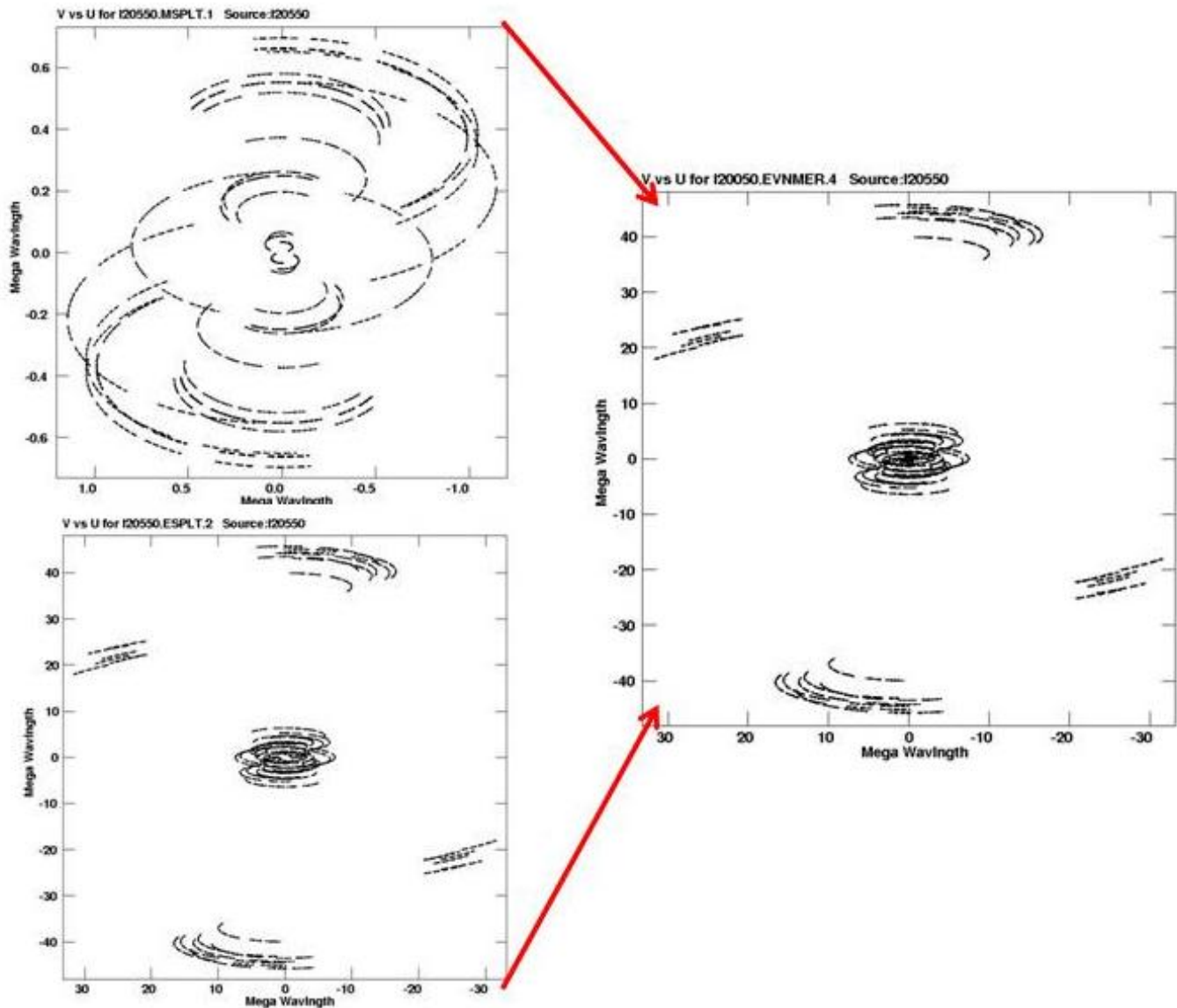
Figure 5.2 The MERLIN and EVN arrays have different uv coverage. This figure demonstrates the different uv coverage capabilities of the arrays and how they can be combined to improve uv coverage. MERLIN has very compact baselines and length, hence more full uv plane. In contrast the EVN has longer baselines that do not covering the entire plane. These plots can be made using UVPLT in AIPS (Cooprider 2010).

VLBI Reduction Process

FITS Files

FITLD – Uploads data into AIPS

POSSM, UVPLT & VPLOT – Evaluate data condition

TACOP – Pipeline tables (FG 1, CL 2 & 3 and BP 1)

TVFLG , IBLED, CLIP – flag bad data by channel, time, etc..

Amplitude Calibration – GETJY, CALIB & SETJY

Phase Calibration – FRING & SETJY

Bandpass Calibration - BPASS

CVEL- Shift spectral line data to common velocity

SPLAT – Separate sources from multi-source data

IMAGR – TVCUB, &TVLOD Image source data

SELF-CALIBRATION – SCMAP or CALIB – Repetitive iterations of the reduction process using the original image as calibrator

KNTR – Contour plots

JMFIT – Gaussian fit

IMEAN – Peak intensity

Figure 5.3 A generalized flow diagram of the reduction process. This applies most directly to EVN observations, but can be adjusted to other data using the AIPS Cookbook (Cooprider 2010).

Chapter 6

Results

We present results for our comparisons between IIZw096, IIIZw035 and ARP220. We wish to emphasize the importance of this study as a preliminary step towards a statistical review of several LIRGS and ULIRGs.

ARP220 and IIIZw035 are two well-known sources that have been observed several times in the radio, optical and even the x-ray. Here we present a brief description of the characteristics and recent studies of these systems in the radio. These results will take into account previous studies by Pihlstrom *et al.*,[26] Diamond *et al.* (1989),[31] and Lonsdale *et al.* (1998),[27] as well as a EVN archival data set of ARP220, taken by Diamond in 2006.

We chose these two studies because they show both compact and diffuse emission which is often considered in characterization. They also have been somewhat resolved and show structure that correlates to both AGN and SBN pumping mechanisms. By classifying these sources in the radio as well as in the optical and IR, we can determine something of their evolution stages. Each of these sources seems to be at a different stage of evolution, which makes them more interesting for source comparison.

In the following few sections we describe the general characteristics of a merging galaxy system, as well as some of the properties of the OHM emission. We then describe a few

45

of the past and current studies regarding the OHM emission, and cite the comparison data set we used to contrast with IIZw096. Lastly we share some of the analysis and results that came from the comparison data set, especially emphasizing the final classification and possible stage of the merger.

6.1 IIIZw035

IIIZw035 is a merging galaxy that has been studied by many people because of its interesting continuum and radio emission structure. IIIZw035 is at a distance of 110 Mpc (z=0.027) and shows characteristics of OHM emission in the central regions of the merger. It is the result of a double galaxy merger comprised of 2 nuclei (see Figure 6.1) with a separation of about 9". The southern nucleus seems to be weaker than the northern nucleus. The northern nucleus shows OHM emission as well as more intense radio continuum and near IR emission.

Previous MERLIN and VLA data showed an unresolved maser spot with a total flux density of about 40 mJy. VLBA and other VLBI observations by Diamond *et al.*(1999)[32] resolved out the continuum and showed an OHM spot. The maser emission seems to be compact and made up of 2 clumps. Trotter *et al.*(1997)[33] suggested that the velocity gradient may be due to VLBI spots blending together. In general this source required higher resolution studies.

Pihlstrom *et al.*(2001)[26] performed MERLIN and EVN observations to achieve the higher resolution. Figure 6.1 and figure 6.2 show some of the results from their paper which is what we used as a comparison data set. The similar resolution and instrumentation allowed us to make a proper comparison between the IIZw096 and IIIZw035 observations.

The EVN-MERLIN contour plot in Figure 6.2 shows compact maser emission in the northern and southern regions. There is also weaker emission in between the two spots, but not in the center. This structure suggests a torus-shaped distribution.
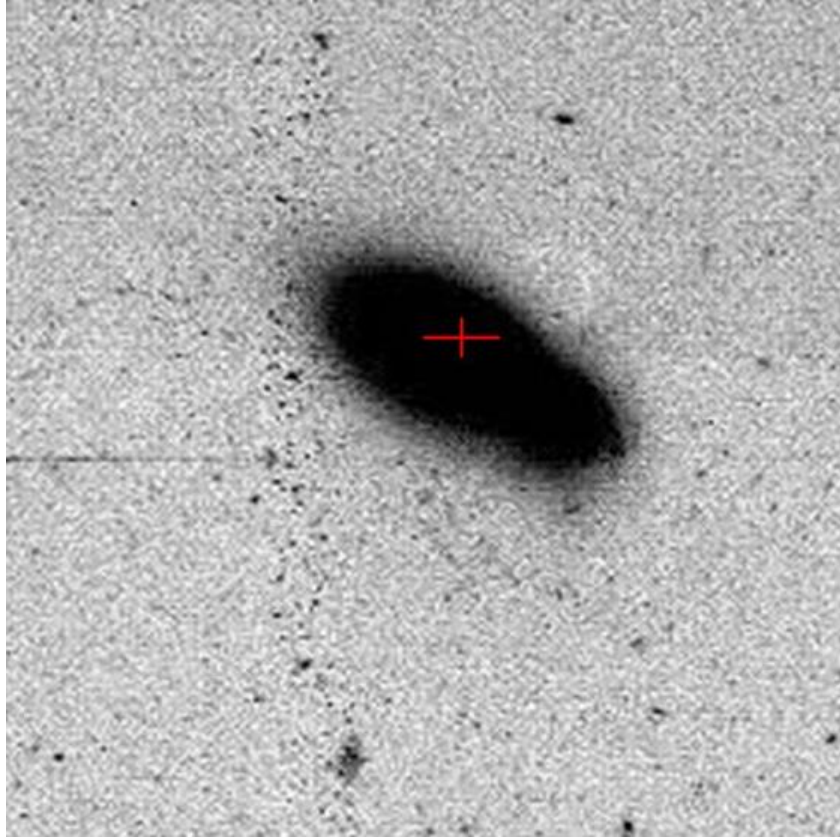
Figure 6.1 HST image of IIIZw035 by Evans *et al.*[34] The cross hatch shows the approximate position of the OHM emission.

Using the velocity (65 km/s) and position offset(44 pc), Pihlstrom *et al.* determined the dynamical mass enclosed within 22 pc to be $7x10^6$ solar masses. In contrast, Sanders *et al.*(1991)[35] used CO observations to derive the molecular mass, which exceeded 10^9 meaning most of the molecular mass was outside the enclosed radius used in the dynamical mass calculation by Pihlstrom *et al.*

The classification from this study by Philstrom *et al.*(2001) came from the continuum emission validated by the radio data. In the optical IIIZw035 showed no signs of AGN components and had high enough IR luminosity (L_{IR}) to be classified as a starburst. From calculations to determine the SFR (19 M_{solar} yr^{-1}) and supernova rate (~ 0.8 yr^{-1}), this classification was confirmed,[26] with the SBN being the mechanism for OH maser pumping
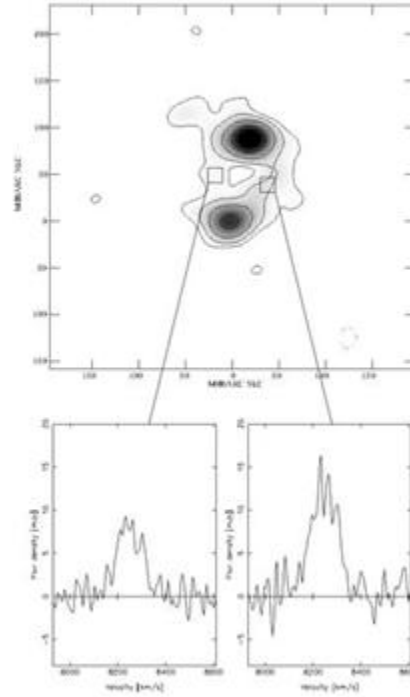
Figure 6.2 EVN and MERLIN radio data of IIIZw035 analyzed by Pihlstrom *et al.*. Figure 6.2 shows the contour plots of the 18-cm spectral data of IIIZw035.[26]

for diffuse emission. The compact emission is the result of supernova remnants (SNR). Although this is contrary to other classifications made by optical observation (Chapman *et al.* 1990),[36] it does present a new understanding of the object. In the Pihlstrom's latest paper (2005) IIIZw035 OHM emission is additionally described as a result of the interaction of radio outflow and molecular material. This outflow may be due to galactic winds which are a consequence of extreme stellar formation. The final classification with radio continuum and IR emission is a starburst nuclei.[37]
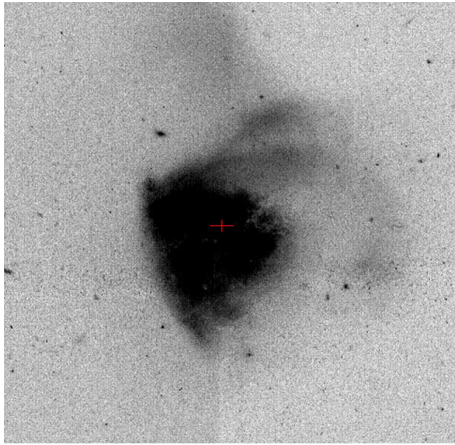
Figure 6.3 HST image of ARP220 by Evans *et al.* 2002.[34] The cross hatch shows the approximate position of the OHM emission.


Figure 6.4 False color HST image of ARP220 by Evans *et al.* 2002.[34]

6.2   ARP220

ARP220 was the first galaxy to be discovered with OHM emission. It has since then been studied in great depth not only in the FIR and radio, but also x-ray. It is at a distance of 74 Mpc (z=0.0181). It is known to have a double-peaked line profile, a few hundred km/s wide, with a high 1667-to-1665 MHz line ratio.[27] There appears to be two nuclear regions which are traced by the maser emission. It shows both diffuse and compact emission in both nuclear regions. Figures 6.3 and 6.4 show the disrupted morphology of ARP220.

Many of the studies of ARP220 have focused on the IR, radio continuum, and optical emission. There is evidence of starburst activity in the outer nuclear region; however, IR observations revealed a compact object deeper within. It has been described as a recent merger, supported by continuum observations by Baan *et al.* (1987).[38] OHM emission in the inner regions of the merger seems to parallel the continuum emission. Diamond *et al.* in 1989 studied the OHM using VLBI observations. Their results showed compact unresolved OHM spots in the inner nuclear regions of the merger. They concluded that there were two compact emission regions corresponding to Seyfert nuclei.[31]

We took these conclusions and looked at more VLBI data, taken by Diamond in 2006. This archival data set seemed to be a second epoch of observations which we compared to past observations by Lonsdale *et al.* (1998).[27] Similar to the EVN archival data Lonsdale *et al.* used 17 VLBI antennas to observe the OHM continuum and spectral structure of ARP220. We used the study by Lonsdale *et al.* and the EVN archival data as comparison data to IIZw096.
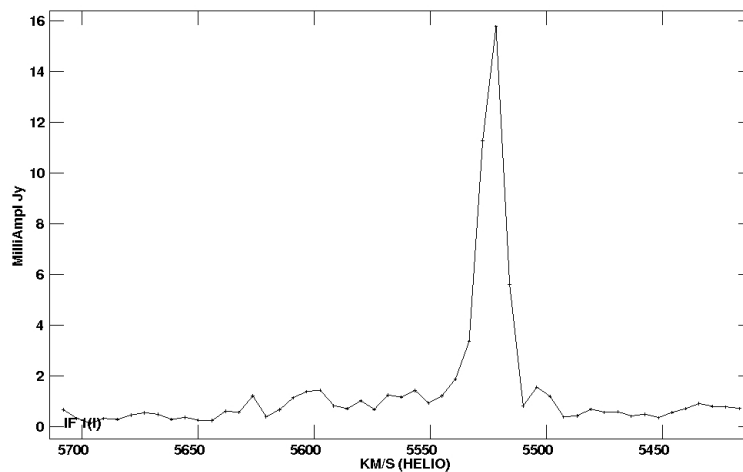
Figure 6.5 Total-power spectrum of ARP220 for the rest frequency 1667 MHz (Cooprider *et al.* 2010, non-published).

The results from the Lonsdale study confirmed two compact regions associated with two nuclei. The compact emission showed elongated structure, linear in nature. The two nuclei are separated by 0.95" in RA and 0.32" in δ.[27] Each compact region is accompanied by a diffuse regions south of the original compact emission. Lonsdale *et al.* concluded that the pumping mechanism for the compact region was either radiative due to starbursting activity or collisional due to a molecular torus orbiting the central mass of an AGN. Their tendency was to speculate an AGN classification because of the saturated compact nature of the OHM emission, but concluded they needed higher sensitivity studies.

However they did conclude in a paper within the same year from a 18-cm continuum

study, that the OHM emission could also be due to starbursting activity. The continuum emission showed properties of SNRs with supernova rates as high as 1.75-3.5 yr^{-1} and SFR of 50-100 solar masses/year.[39]
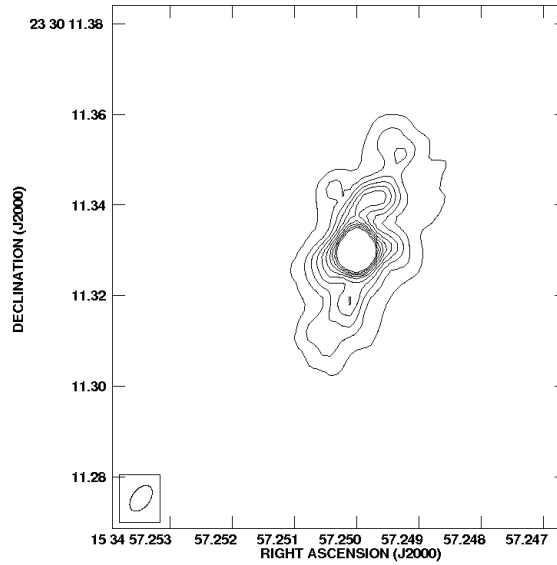
Figure 6.6 Average of several velocity channels. The Western compact OHM emission in ARP220. Shows linear elongated structure as mentioned by Lonsdale *et al.*[39] 1998. Our reduction from the EVN archive (Cooprider 2010, non-published)

The EVN archival data confirmed similar compact elongated structures in two nuclei (See Figures 6.6, 6.7 and 6.8). We reduced this data not to find differences in the conclusions of Lonsdale *et al.*, but to simply confirm their findings. Similar to IIIZw035, Lonsdale concluded that the OHM emission was either diffuse or compact, where the compact regions were saturated and dependent on either AGN or SBN as the pumping mechanism (Figures 6.7 and 6.8). AGN as the pumping mechanism indicates a young merger, because the galaxies have not had enough time to disrupt the initial AGN structure. This OHM source seems to show properties of both AGN and starburst.[39]
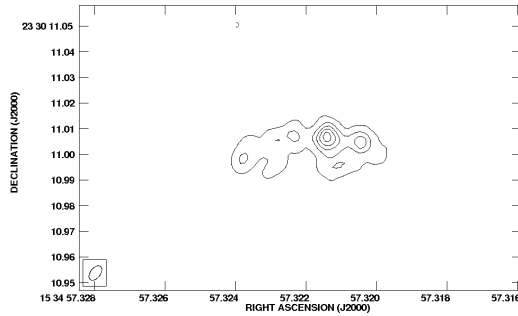
Figure 6.7 Average of several velocity channels. The Eastern compact OHM emission in ARP220 (Cooprider 2010, non-published).
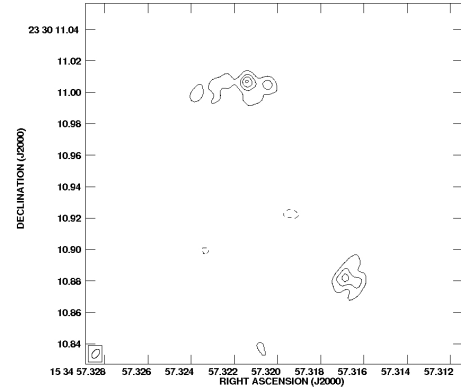
Figure 6.8 Average of several velocity channels. The Eastern compact and diffuse OHM emission in ARP220 (Cooprider 2010, non-published).

6.3 IIZw096

Because IIZw096 is the focus of this study we will describe more specifically the recent studies of this system. This includes the radio, optical, x-ray and IR observations.

IIZw096 was one of the several sources detected in the Giovanelli and Darling OHM survey.[40] Optically it shows a relatively interesting morphology, with the possibility of 2-3 galaxies present in the merger (see Figures 6.9 & 6.10). It has an infrared luminosity of $\log(L_{IR}/L_{solar}) = 11.94$. In 1997 Goldader *et al.*[41] using near-infrared imaging and spectroscopy, observed two extremely red sources to the east of the merging disks. They suggested that these red sources were highly obscured young starbursts which occurred before the final onset of dissipative collapse. This conclusion arguably classifies IIZw096 as a late stage merger.

IIZw096 was also observed using the VLA by Bann & Klockner (2006),[42] as part of a 51-source survey. The radio properties of the system were compare with the optical line properties to set its classification as a starburst (See Appendix A).

Recently a study by Inami *et al.* (2010)[43] focused on IR, optical, UV, and x-ray emission from this source. IIZw096 was one of many sources in a study of several LIRGs in
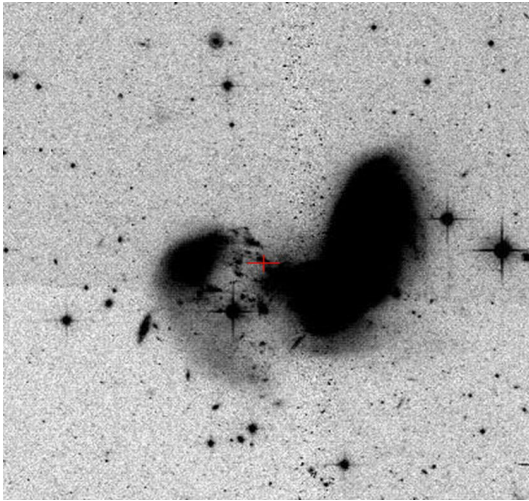
Figure 6.9 HST image of IIZw096.[34] The cross hatch shows the approximate position of the OHM emission.

Figure 6.10 False color HST image of IIZw096 showing the extremely complicated morphology and multiple nuclei.[34]

a survey called Great Observatories All-sky LIRG Survey (GOALS). Their study focused on observations from the Spitzer Space Telescope, Hubble Space Telescope, Chandra X-ray Observatory, and AKARI Infared Astronomy Satellite.

The Spitzer observations revealed 80 percent of the FIR emission came from the off-nuclear region (see Figure 6.11), where the starburst is theorized to exist. The IR luminosity in this region predicts a SFR of $120 M_{solar}/year$. The HST (NICMOS) observations enhanced the red sources, showing up to 10 red "knots", the brightest knot correlating to where most of the FIR emission was found. The Chandra X-ray observations also place the hardest source in the same region, between the first and second most intense red knots. Additionally Spitzer IRA and AKARI spectra predict a starburst dominated system because of the existence of PAH. The ratio of F_{PAH}/F_{IR} is equal to 0.02, which on the low end for pure starburst activity. In the region of the most intense FIR radiation, assuming an extinction in the H band of 3.3 mag and the solar metallicity they estimated the mass to be on the order of $10^9 M_{solar}$.[43]

We add to this new analysis of IIZw096, San Pedro Martir optical results and high
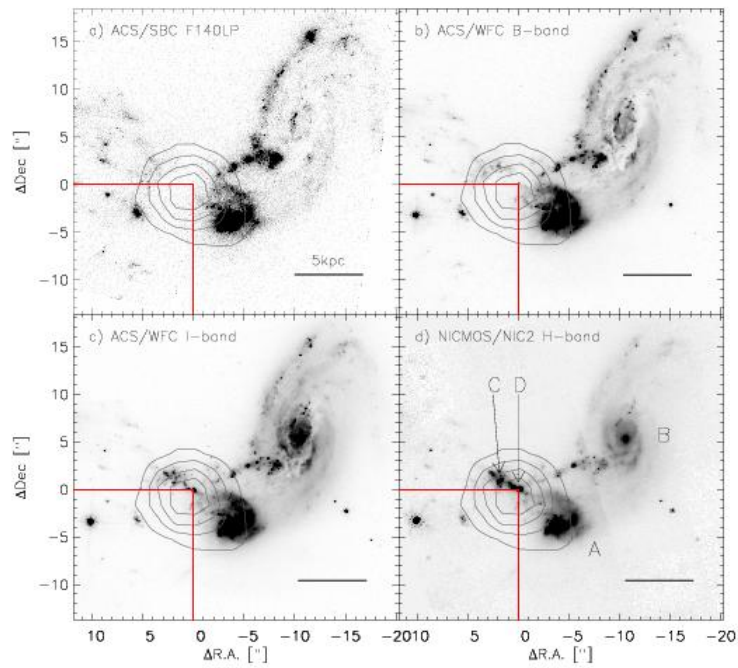
Figure 6.11 HST/ACS and NICMOS as grayscale with Spitzur 24 micron contours overlaid. The map is centered at the regions of the highest IR emission.[43]

resolution radio data taken using the MERLIN and EVN arrays. We will introduce briefly, describe and deduce information from each image.

6.3.1   BVRI and H_α Observations

The BVRI image (right image in Figure 6.12) shows the regions where the older and younger populations may reside. The redder regions correspond to an older, higher metallicity population. The bluer regions correspond to younger hot stars, where stellar formation is more prevalent. This image shows two regions near the center of the merger where younger populations seem to be the most intense. These regions would be the most likely candidates for OHM emission. There is a region in the central part of this image that shows a reddish spot. As has been measured previously by Coziol *et al.*, this spot is not a consequence of extinction or reddening, but possibly high-energy photons from an AGN core or extremely obscured and intense starburst activity.[3]
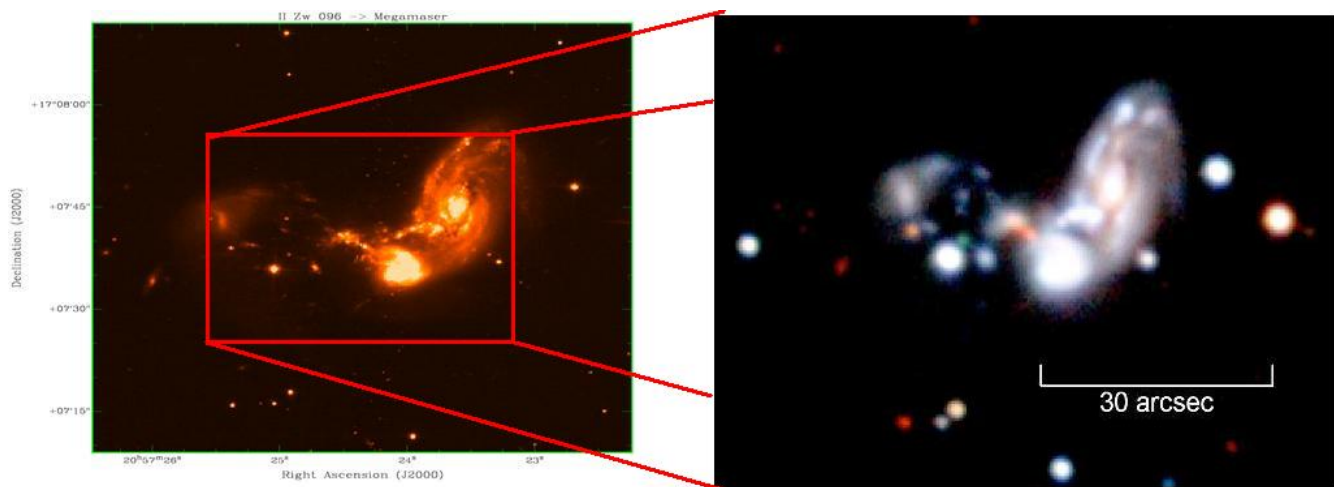
Figure 6.12 HST[34] image of IIZw096 showing where BVRI[3] filtered image fits within the merging galaxy landscape.

In H_α regions hot gas from supernovae would initiate stellar formation, possibly in great bursts. The circles in Figure 6.13 highlight the regions of most intense stellar formation. This image, compared with the BVRI image, shows where the most possible star formation is likely occurring, and hence where the OHM is present. In the case of IIZw096, the OHM emission is found in circle C, where the 2nd most intense region of H_α is measured. This is
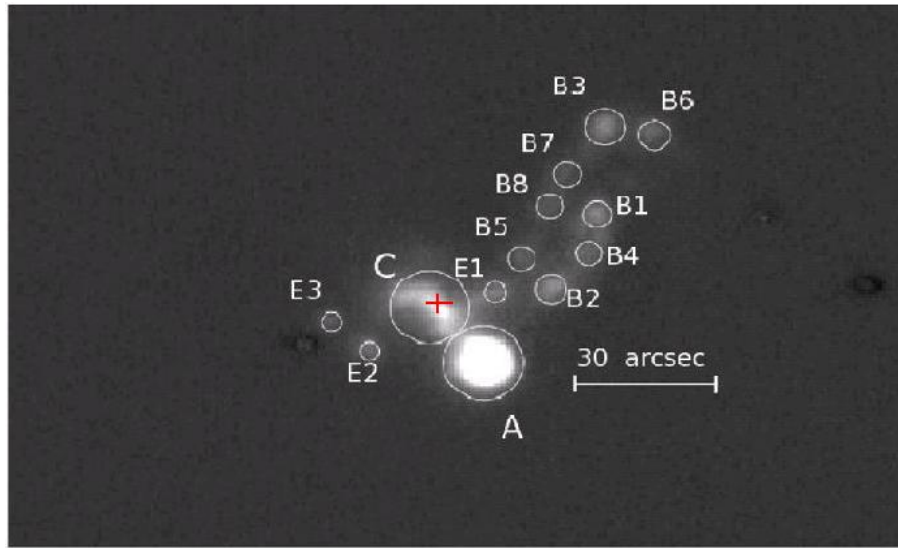
Figure 6.13 H_α image of IIZw096, with circles that identify the most intense regions of star formation in this merging system.[3] The cross hatch shows the approximate position of the OHM emission.

also where the red region resides in the BVRI image. In Table 6.1 Coziol *et al.* calculated the star formation rates[44] from the fluxes found in the H_α image.

Table 6.1.   Hα intensity in terms of star formation rates.[3]

Id. Region	$L_{H\alpha}$ $\times 10^7 L_{\odot}$	$Log(L_{H\alpha})$	Radius kpc	SFR $M_{\odot}$ yr^{-1}
A	37.8	8.6	2.9	11.3
B1	9.0	8.0	1.9	2.7
B2	8.9	8.0	1.8	2.7
B3	8.8	7.9	1.4	2.6
B4	8.8	7.9	1.6	2.6
B5	8.7	7.9	1.6	2.6
B6	8.2	7.9	1.2	2.5
B7	7.7	7.9	0.9	2.3
B8	7.7	7.9	1.2	2.3
C	36.3	8.6	2.5	10.9
E1	10.7	8.0	1.4	3.2
E1	8.1	7.9	1.4	2.4
E2	7.7	7.9	1.1	2.3

6.3.2   MERLIN Observations
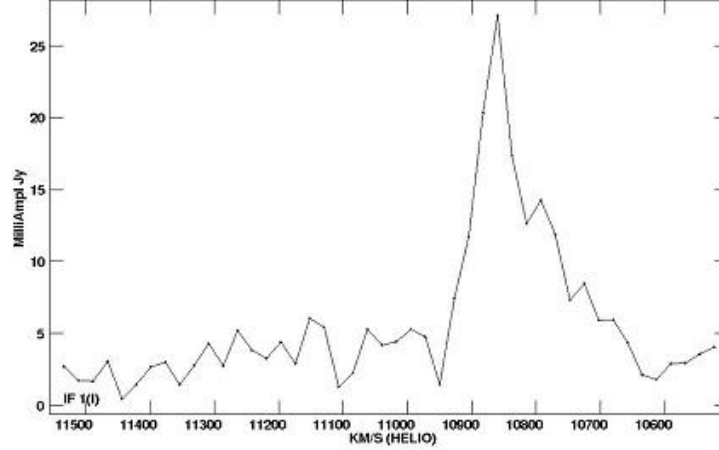
Figure 6.14 OHM emission spectrum taken from MERLIN data. Shows slight spectral resolution (Coziol *et al.* To be published 2010).

The MERLIN radio data gave us a first understanding of the nature of the OHM emission in IIZw096. The spectrum shows the emission to peak at 1667 MHz. We had 64 velocity(frequency) channels, the peak emission occurring at the velocity 10860 km/s because of the offset for detecting emission at 1665 MHz(see Figure 6.14).

As seen in the image Figure 6.15, the OHM spot is elongated, and larger than the beam, even over several velocity channels. We were able to determine the position to be α: 20 57 24.37517 $\pm$ 0.00005, δ: 17 07 39.1748 $\pm$ 0.0009, the position angle: $30^0.826 \pm 0^0.442$, and the peak intensity: $1.50 \times 10^{-02} \pm 1.16 \times 10^{-04}$ Jy/beam. There is a velocity gradient across the channels of emission which indicate that MERLIN is barely resolving a second spot.

From these data, where the velocity range for the OHM emission is 200 km/s, and from the optical measurements, where the region is 300 pc in size, we determined the mass in the central regions of the galaxy merger to be on the order of $10^9 M_{solar}$. The mass calculation comes from assuming a Keplerian bounded system where $M = \frac{v^2 D}{G}$.

We assumed M as the total mass enclosed in the 300-pc region, v as the velocity range observed from OHM spectral emission, $D = \theta R$, (where R is the distance to the source and
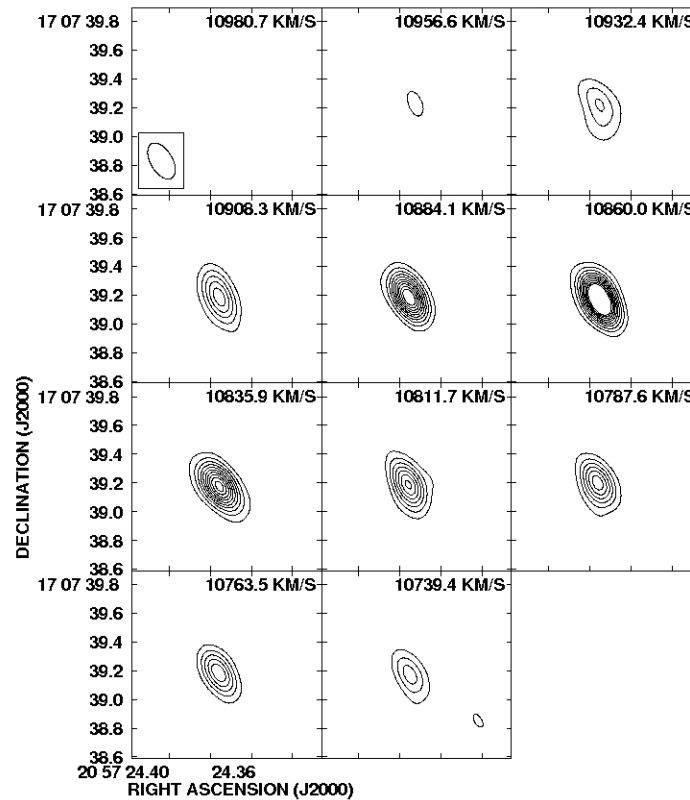
Figure 6.15 Contour map of the OHM emission of IIZw096, frequency channels 35-45. MERLIN data shows an elongated shape, slightly larger than the beam showing some resolution of the structure (Coziol *et al.* To be published 2010).

θ is a function of the beam width) and G as the gravitational constant. This calculation of mass applies more to an AGN core than to an SBN. This is in conflict with previous optical studies classifying this object as only an SBN.

We also looked at the velocity gradient, using JMFIT to plot the α and δ shift over each channel. The only velocity changed appeared in the RA. Most importantly the MERLIN data confirms that there is a double structure hardly resolved with the limited resolution of the MERLIN array, and no real velocity gradient. The velocity-RA plot from the MERLIN data shows an almost sinusoidal shape which depicts the existence of two spots the smaller

of the two more apparent at higher frequencies. We checked these results with the EVN data, which showed no change in velocity over RA. Figure 6.16 shows the velocity change over RA. We do not show a similar plot for the EVN because it there was not a significant change.
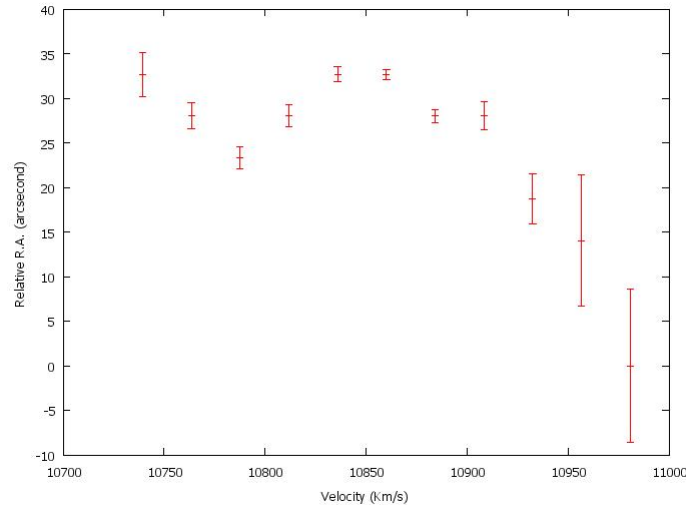
Figure 6.16 Velocity gradient in MERLIN confirms the existence of a double structure seen in the EVN observations (Cooprider 2011).

6.3.3 EVN Observations

Because we did not have sufficient spectral and spatial resolution to determine Zeeman or double spot structure, we utilized EVN data to try to resolve these issues.

The data from the EVN array allowed us to attain better spectral and spatial resolution so that we could determine more about the structure of the spot. We increased the spectral resolution from 64 to 256 velocity channels. With 64 channels each channel covered approximately 24 km/s, with 256 (see Figure 6.17) channels each channel covered approximately 6 km/s. When covering a range of 1500 km/s, increasing the number of channels improved the spectral resolution by a factor of four.

The contour plots also show the same elongated shape (see Figure 6.18) as seen from the
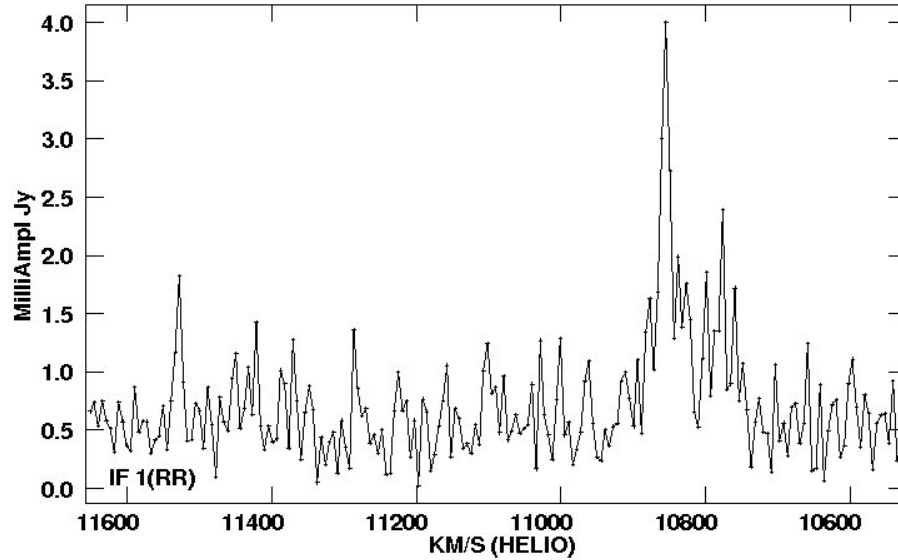
Figure 6.17 OHM emission spectrum of IIZw096 taken from EVN data (Cooprider 2011).

MERLIN data. The data initially showed the potential for two spots, the second northern spot having a lower intensity, where both are partially resolved. The second spot appears at a different velocity which may correlate to a doppler shift of the OHM emission. The low signal to noise ratio of the smaller spot indicates that this spot is hard to self-calibrate. Unfortunately with the baselines from the EVN, we still have not resolved much structure. We were able to determine the position to be α: 20 57 24.375192 $\pm$ 0.000009, δ: 17 07 39.1448 $\pm$ 0.0002, the position angle:$14^0.625 \pm 1^0.272$, and the peak intensity: 3.28×10^{-03} $\pm$ 7.48 $\times$ 10^{-05} Jy/beam. Because the EVN has better resolving power we found more accurately the position of the OHM spot.

To increase the u-v coverage the first EVN data set was combined with the MERLIN data. This increased the sensitivity of the data observations. The EVN-MERLIN data showed more nearly circular spots (see Figures 6.19 & 6.20) without much better resolution than the EVN. We were able to determine the position to be α: 20 57 24.375070 $\pm$ 0.000004, δ: 17 07 39.14630 $\pm$ 0.00006, the position angle: $158^0.411 \pm 1^0.783$, and the peak intensity: 1.90 $\times$
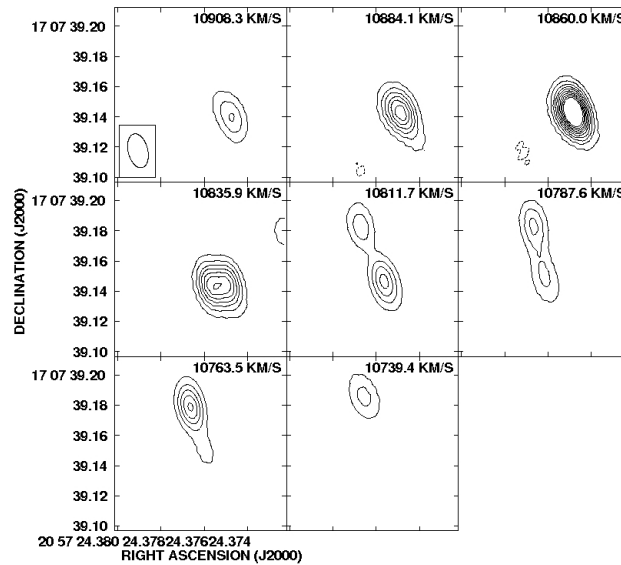
Figure 6.18 Contour plot of the OHM emission of IIZw096 taken from EVN data, frequency channels 35-45. Shows structure that correlates to the elongated structure found by MERLIN observations.There is also a second spot that appears at the higher channels (higher frequency)(Coorpider 2011)
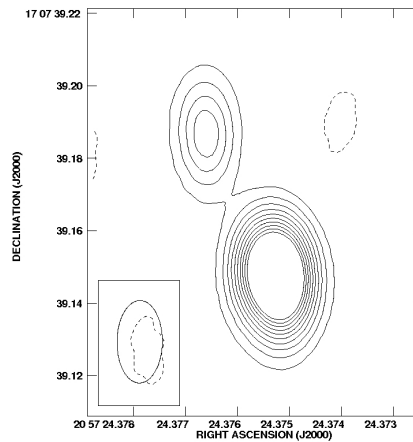
Figure 6.19 Contour plot of OHM emission of IIZw096 averaged over several velocity channels, showing the double nature (Cooprider 2011).

$10^{-02} \pm 1.25 \times 10^{-04}$ Jy/beam. Without resolution we cannot make definite determinations of motion, however we can say something about the position with respect to the optical information.

We expect another EVN 18-cm data set within the next couple months. The observations
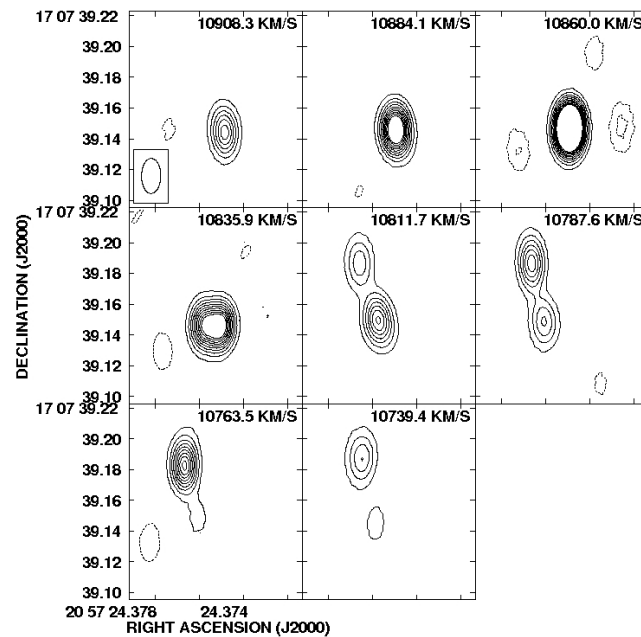
Figure 6.20 Contour plots over 11 velocity channels of OHM emission in IIZw096, showing the second spot that appears at higher frequencies (Cooprider 2011).

were taken on June 6, 2010 which is 6 years after the previous observations. Both sets of observations could potentially show proper motions confirming the assumed structure of the OHM emission.

6.3.4   GOALs with Radio Results

Our intention to make this a multi-frequency study of LIRGs is accommodated by the GOALS survey. Here we compare the positional information from the radio observations with the FIR, x-ray and optical results from the Inami *et al.* paper (2010).[43]

With our high resolution radio data we were able to determine more accurately the position of the OHM emission. By comparing it with the HST, Spitzur and Chandra observations we found that the OHM emission was all within the most intense region of FIR emission, part of the red knot structure found outside the nuclear regions of the merger. In the GOALS study of IIZw096, they named the region of highest FIR emission spot D. The α and δ for

this source $20^h57^m24^s.34$ and $17^007'39''.1$ respectively. Using the most accurate position for the MERLIN+EVN observations, the difference between the α is on the order of 0.01" and the δ is within the same range to the first decimal place.

From the NICMOS image (see Figure 6.21) the region D size is on the order of 0.5 arcseconds (width), much larger than the difference in our positional measurements. This confirms that the OHM emission is in fact within the region of highest FIR intensity and, more importantly, associated with the highly obscured extreme starburst activity or possibly an obscured AGN. Region D is also where there are hard x-rays found.
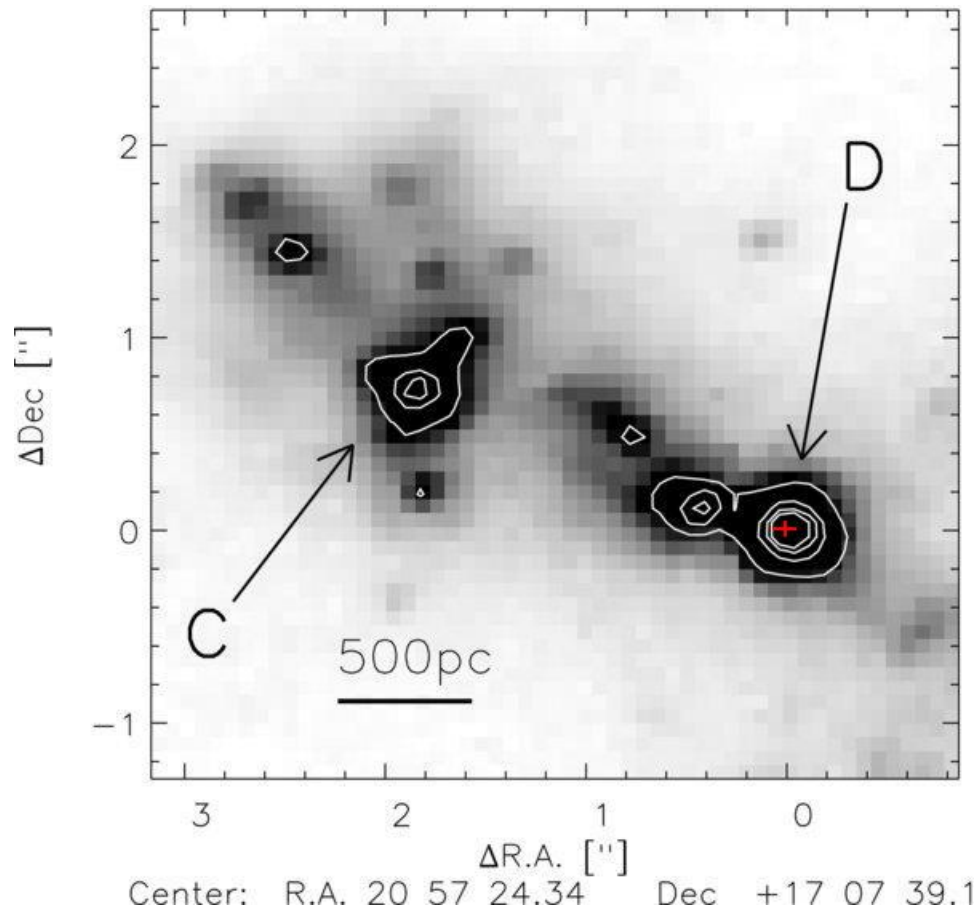
Figure 6.21 Magnified NICMOS image of IIZw096, identifying the red sources("knots"), and the D spot as the most intense region in the FIR. The map is with the region D, where the OHM emission also resides[43] .

The unclear classification of IIZw096 suggests the existence of both AGN and SBN, a

composite. Darling and Giovanelli study site at least 8 other sources with a similar classi-fication.[40] Comparing the optical morphology, FIR luminosity and radio OHM structure of these sources with IIZw096 would be an interesting and needful comparison to aid in the classification of IIZw096.

Chapter 7

Conclusions

7.1   Comparison of IIZw096, IIIZw035 and ARP220

IIZw096 has just recently become a more interesting source to study, not only because of its unique optical morphology, but also because of the intense FIR emission not associated with the nuclear regions of the merger. The high resolution radio data confirms that this region has a high density and a high mass.

IIIZw035, which shows both continuum and spectral radio emission[26] and shows more of a disk structure which correlates to a double structure in the radio but does not necessarily compare to the double seen from the observations of IIZw096. The double structure of the OHM in IIZw096 may correspond more accurately to the red knot structure found in the NICMOS observations by Inami (2010). IIIZw035 also shows a continuum structure that is similar in morphology to that of the spectral emission. In the case of IIZw096, it is too distant to resolve the radio continuum. Both these sources, though having very different geometries, are speculated to be due to starburst activity because radio continuum confirms SNR existence.

ARP220, which shows a more complicated OHM radio emission, is different because of

the region in which the emission occurs. In contrast to IIZw096, whose emission occurs outside the inner nuclear regions, APR220's emission is found in the two nuclear regions of the merger. The compact emission is said to trace the shock fronts of the AGN cores. The elongated structure of the OHM emission in ARP220 may correspond to regions shocked by the passage of twin jets.[27] Because the OHM emission is shown to emit outside the nuclear regions of the merger, we cannot assume a similar situation. Additionally, the red spot with a seemingly high mass, has been cited by NICMOS observations[43] as a knot structure of starburst activity and not that of AGN jets.

Both IIIZw035 and ARP220 show diffuse and compact OHM emission. In ARP220 the diffuse emission (unsaturated) appears to be a result of IR radiation pumping, and the compact emission (saturated) a result of shock fronts stemming from the nuclear regions of the merger. The OHM emission in IIIZw035 also shows diffuse emission which is theorized to be a result of electrons accelerated by supernova remnants, and compact emission which is believed to be driven by from powerful clusters of young supernova remnants, primarily associated with starbursts. With limited resolution, IIZw096 only shows two compact regions which seem to correlate to starburst activity. However, in that region the mass is high enough to be an AGN core.

All studies show that high sensitivity and high resolution is needed to gain more information about each source. The radio observations are resolution limited even though all of these sources have been observed using the VLBI networks.

7.2 Final Conclusions

IIZw096 is not the first OHM source where there have been some discrepancies in its classification. This project focused on the radio emission and how it correlated to the optical and environmental results. The following were the most important results of this project:

1. IIZw096 showed characteristics similar to IIIZw035 and ARP220. Much like IIIZw035 it did not show significant radio continuum at higher resolution and showed an elongated structure similar to that of ARP220. The elongated structure of ARP220 coincides with the nuclear regions of the merger. In IIZw096 the compact activity that is NOT within the nuclear regions of the merger.

2. Our calculation of the mass within a 300 pc region of 10^9 solar masses is sufficient for the existence of an AGN and agrees with the calculations of mass in current study by Inami *et al.*(2010). This is also where the OHM emission is found.

3. The H_α data indicates that source A is clearly a starburst, but the OHM is associated with our region C (D in the paper by Inami *et al.*). If OHM were only associated with starburst it would be found in source A and C. This suggests the need for something besides starbursts to initiate maser pumping.

4. According to the EVN and MERLIN data, the maser spot has been slightly resolved and shows an elongated shape with possibly two spots visible at 1667 MHz. Because IIZw096 is at a farther distance than both IIIZw035 and ARP220 this may mean that it requires the largest observational baselines, which in the case of this study have not been completely achieved. With another set of 18-cm radio data we should be able to confirm the OHM structure and use proper motion studies to understand the environment of the emission.

5. Using the positional information from the EVN+MERLIN data, the OHM spots are located in region C (D in the NICMOS[43]image) where the 2nd most intense H_α is found and the most intense FIR is found. This is also the same region that shows hard x-rays, a characteristic of AGN activity.

6. The study by Darling and Giovanelli (2002)[40] sites the existence of a composite AGN

and SBN classification. This is a possible classification for IIZw096 which seems to shows characteristics of both.

7. Statistically, this may seem insignificant, however there are several more sources that should be studied which are also part of the Giovanelli and Darling survey. Several of these studies are under investigation, and have been cited in the newest proposal for later this year.

Bibliography

[1] W. A. Bann, ASP Conf Ser 16 p. 45 (1991).

[2] D. B. Sanders and I. F. Mirabel, "Luminous Infrared Galaxies," ARA & A **34,** 749–92 (1996).

[3] I. P. F. J. M. I. K. C. L. R.-G. R. Coziol, V. Migenes and H. R. Klockner, "Optical and OH Megamaser observations of the starburst galaxy II Zw 096," To be published (2010).

[4] B. W. C. D. A. Ostlie, "Modern Astrophysics," Addison-Wesley Publishing Company Inc. (1996).

[5] C. Digest, "Starburst Galaxies,", 2010.

[6] R. Antonucci, "Unified Models for Active Galactic Nuclei and Quasars," Annual Review **31,** 473–521 (1993).

[7] K. et al., ApJ **556,** 121–140 (2001).

[8] T. S.-s. L. Kwok-san, "What is a Laser?,", 2010.

[9] M. Elitzur, "Astronomical Masers," Spring Publishing (1992).

[10] M. J. Reid and J. M. Moran, "MASERs," Ann Rev Astron. Astrophysics **19,** 231–76 (1981).

[11] P. D. L. Matveyenko and D. Graham, Astronomy Letters **24,** 623–631 (1998).

[12] R. A. B. S. H. Knowles, "Linear Polarization of 22-GHz water-vapour line emission in southern sources," Royal Astronomical Society, Monthly Notices **184,** 107–117 (1978).

[13] C. Lonsdale, "OH Megamasers," IAU Symposium 206 (2002).

[14] H. E. H. Scheffler, "Physics of the Galaxy and Interstellar Matter," Spring-Verlag p. 58 (1988).

[15] A. Pacholczyk, "Radio Astrophysics," W. H. Freedman and Company pp. 185–187 (1970).

[16] A. E. R. R. Coziol, V. Migenes and M. A. Trinidad, VLA proposal (2004).

[17] R. C. M.A. Moreno-Corral and W. Schuster, "San Pedro Martir," (194).

[18] T. Reichhardt, "Nations wrestle to host future telescope," Nature **439,** 377 (2006).

[19] F. Ghigo, "Karl Jansky and the Discovery of Cosmic Radio Waves,", 2010.

[20] A. R. Thompson, "Fundamentals of Radio Astronomy," Ninth Synthesis Imaging Summer School **ASP Conference Series 180,** 11–36 (2004).

[21] R. Perley, "Fundamentals of interferometry," Ninth Synthesis Imaging Summer School (2004).

[22] NRAO, "VLA,", 2010.

[23] E. V. Network, "EVN array,", 2010.

[24] U. of Manchester, "MERLIN/VLBI National Facility,", 2010.

[25] C. C. R.C Walker, G.B. Taylor and R. A. Perley, "Very Long Baseline Interferometry," ASP Conference Series **180,** 433–462 (1999).

[26] R. B. P. D. Y. Pihlstrom, J. Conway and A. Polatidis, "EVN and MERLIN Observation of III Zw 035: A starburst continuum and an OH maser ring," A & A **377,** 413–424 (2001).

[27] P. D. C. Lonsdale, C. Lonsdale and H. Smith, "Symmetric Parsec-scale OH Megamaser Structures in ARP 220," Astrophysical Journal **493,** L13–L16 (1998).

[28] W. J. Schuster and L. Parrao, "The Atmospheric Extinction of San Pedro Martir," Revista Mexicana de Astronomia y Astrofisica **37,** 187–200 (2001).

[29] N. R. A. Observatory, "AIPS Cookbook," NRAO p. Ch 9 (2009).

[30] S. M. A. Biggs, "EVN Data Analysis Guide," JIVE 2.4 (2008).

[31] P. Diamond, "Very Long Baseline Interferometry II: The Techniques of Spectral Line VLBI," Third NRAO Synthesis Imaging Summer School **6,** 379 (1989).

[32] C. L. . H. S. P.J. Diamond, ApJ **511,** 178 (1999).

[33] L. G. X. Z. . C. G. A.S. Trotter, J.M. Moran, ApJ **485,** L79 (1997).

[34] E. H. H. A. Evans, NASA, "HST data proposal 10592,", 2008.

[35] C. L. . P. D. D.B. Sanders, C.J. Lonsdale, ApJ **370,** 158 (1991).

[36] D. A. e. a. J.M. Chapman, L. Staveley-Smith, MNRAS **244,** 281 (1990).

[37] Y. Pihlstrom, "OH Megamasers Galaxies at High Angular Resolution," ASP Conference Series 340 (2005).

[38] J. S. . I. F. M. W. A. Bann, J.H. Van Gorkom, ApJ **313,** 102 (1987).

[39] C. J. L. . P. J. D. H. E. Smith, C. J. Lonsdale, "A Starburst Revealed: Luminous Radio Supernovae in the Nuclei of Arp 220," Nature 493 (1998).

[40] J. Darling and R. Giovanelli, "A Search for OH Megamasers as z>0.1. III. The Complete Survey," AJ 124 (2002).

[41] R. D. J. R. D. . D. B. S. J. D. Goldader, D. L. Goldader, AJ **1113,** 1569 (1997).

[42] W. A. Bann and H. R. Klockner, "Radio Properties of FIR-megamaser nuclei," A&A **449,** 559–568 (2006).

[43] I. et al., "The Buried Staburst in the Interactinn Galaxiy II Zw 096 as Revealed by the Spitzur Space Telescope," ApJ **140,** 63–74 (2010).

[44] C. S. B. . S. D. R. Coziol, MNRAS **276,** 1245 (1995).

[45] J. J. S. W. A. Baan and R. D. LeWinter, "Optical Classification of Megamaser Galaxies," The Astrophysical Journal **509,** 633–645 (1998).

Appendix A

Tables

This appendix includes 3 studies including the Giovanelli and Darling study of all three sources. It is for reference purposes.

Table 1A.   Source Name and General Information

Source	RA (Hours)	DEC (Degrees)	z (redshift)	Freq (GHz)	Peak Flux (mJy/Beam)
IIZW096	20:55:05.3	+16:56:02.4		4.8	3.21
IIIZW035	01:41:47.91	+16:51:06.3	0.03	8.4	13.7
ARP220	15:32:46.95	+23:40:07.7		8.4	28.5

References. — Baan & Klockner 2006[42]

Table 1B.   Source Structural Characteristics

Source	Total Intensity (mJy)	Size (arcsecxarcsec)	PA (degrees)	rms (mJy/beam)
IIZW096	6.57	1.07x0.54	63	0.22
IIIZW035	19.3	0.18x0.14	-	0.03
ARP220	60.7	0.32x0.19	-	0.03

References. — Baan & Klockner 2006[42]

Table 1C.   Source FIR Characteristics

Source	F60 (Jy)	F100 (Jy)	Radio Bands	FIR Luminosity (Log(Lsolar))
IIZW096	13.3	10.6	LC	11.6
IIIZW035	12.6	13.3	LX	11.36
ARP220	103.8	112.4	LX	11.9

References. — Baan & Klockner 2006[42]

Table 1D.   Final Classifications

Source	Nuclear Code (NC)	Activity Factor (β)	Optical Class	Final Class
IIZw096	0	0.78	SB	S
IIIZw035	100	-0.14	L	AGN
ARP220	100	0.02	S2	S

References. — Baan & Klockner 2006[42]

Table 2A.   Optical Characteristics (cHB 3 Balmar decrement redding parameter)

Source	mB	cHB	$Log([OIII]/HB)$	$Log([OII]/HB)$	$Log([NII]/HB)$
IIZW096	15.2	0.59	0.33	0.47	-0.69
IIIZW035	14.5	2.81	0.47	1.93	0.04
ARP220	14.4	2.9	0.64	1.9	0.24

References. — Baan & Salzar 1998[45]

Table 2B.   Optical Classifications

Source	$Log([OI]/HB)$	$Log([SII]/HB)$	Type
IIZW096	-1.56	-0.75	SBN
IIIZW035	-0.57	-0.23	LINER
ARP220	-0.54	-0.19	Seyfert

References. — Baan & Salzar 1998[45]

Table 3A. Radio and FIR Characteristics

Source	Velocity(Solar) (km/s)	Velocity(CMB) (km/s)	f60 (Jy)	f100 (Jy)	log(FIR Lsolar) ($h75^{-2}$ Lsolar)
IIZW096	10822	10517	13.28	10.57	11.56
IIIZW035	8245	7952	12.55	13.31	11.32
ARP220	5426	5545	103.8	112.4	11.92

References. — Darling & Giovanelli 2002[40]

Table 3B. Radio and FIR Classifications

Source	logLOH(prod) ($h75^{-2}$ Lsolar)	logLOH ($h75^{-2}$ Lsolar)	f1667 (mJy)	f1.4GHz (mJy)	Class
IIZW096	1.93	2.13	40	43.9	H(1)
IIIZW035	1.6	2.65	240	40.6	L(1),H/L(3),H/A(4)
ARP220	2.43	2.59	280	326.8	S2(1),L(3,7)

References. — Darling & Giovanelli 2002[40]

Appendix B
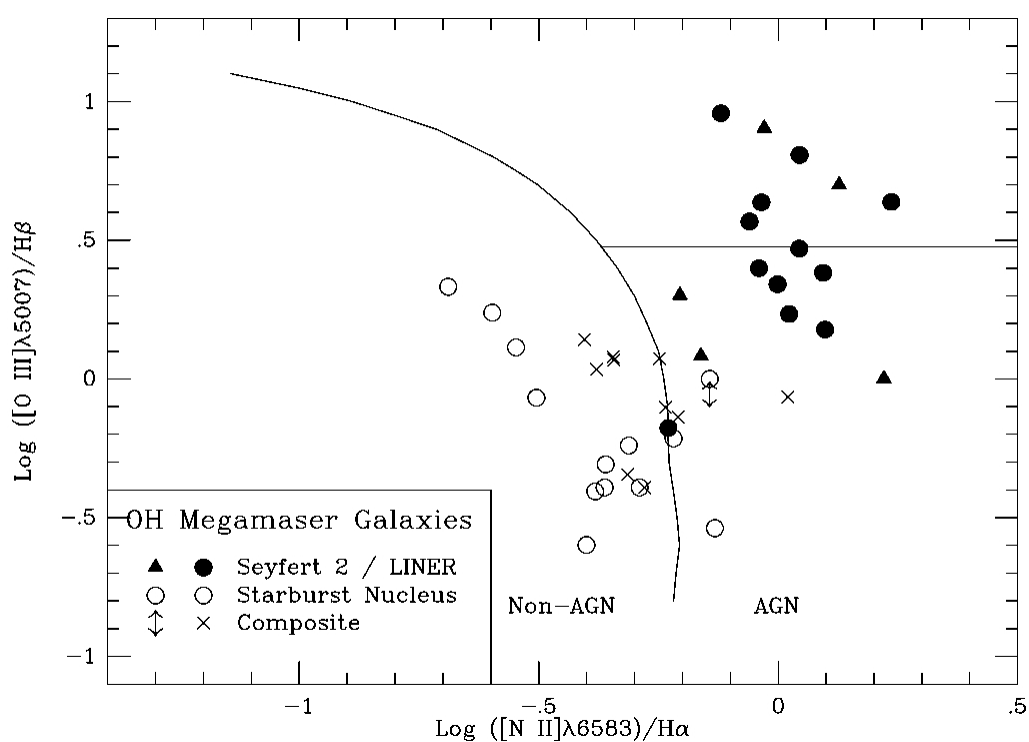
Diagnostic Diagram

This table and diagram is the original diagnostic diagram classifying Megamaser objects as AGN, SBN or composite sources by Baan *et al.*(1998).[45] The diagnostic diagram with this thesis is a modified version of the same source from this study. T0 is similar to the classification of composite and the HII regions signify starburst activity or SBN.

PSC Name (1)	Other Names (2)	R.A. (1950) (3)	Decl. (1950) (4)	m_B (5)	z (6)	Comments (7)
IR00057+4021......		00 05 45.0	40 21 13	15.5	0.0443	
IR00335−2732......		00 33 31.9	−27 32 04		0.0687	
IR01364−1042......	IC 766	01 36 24.1	−10 42 24		0.047	Not observed
IR01418+1651......	III Zw 35	01 41 48.1	16 51 07	14.5	0.0274	
IR02483+4302......		02 48 20.4	43 02 56	15.5	0.0510	
IR03056+2034......		03 05 38.3	20 34 56		0.0271	
IR03260−1422......		03 26 04.6	−14 22 25	15.0	0.0427	
IR04332+0209......		04 33 12.3	02 09 24	15.0	0.0117	
IR05100−2425......		05 10 05.2	−24 25 29	15.0	0.0332	
IR05414+5840......	U 3351	05 41 25.6	58 40 51	16.0	0.0147	
IR06206−3646......		06 20 40.2	−36 46 10		0.108	Not observed
IR08071+0509......		08 07 08.7	05 09 59		0.0520	
IR09320+6134......	U 5101	09 32 04.7	61 34 37	15.5	0.0392	
IR10039−3338......		10 03 54.8	−33 38 43	14.9	0.034	Not observed
IR10173+0828......		10 17 22.0	08 28 40	15.0	0.0489	
IR10378+1109......		10 37 49.1	11 09 08		0.136	Not observed
IR10485−1447......		10 48 34.6	−14 47 27		0.133	Not observed
IR11010+4107......	Arp 148	11 01 05.8	41 07 08	15.5	0.0349	
IR11069+2711......	IC 2626	11 06 56.9	27 11 23		0.0703	North component
IR11257+5850......	IC 694, Mrk 171	11 25 42.1	58 08 18	12.6	0.0100	2 nuclei observed
IR11506−3851......	ESO 320−20	11 50 40.2	−38 51 10	15.0	0.009	Not observed
IR12018+1941......		12 01 51.8	19 41 46	16.5	0.1677	
IR12112+0305......		12 11 12.2	03 05 21	16.0	0.0730	
IR12243−0036......	N 4418	12 24 22.1	−00 36 14	14.2	0.0073	
IR12540+5708......	Mrk 231	12 54 04.7	57 08 39	14.1	0.0419	
IR13097−1531......	N 5010	13 09 46.6	−15 31 58	15.0	0.0097	
IR13126+2452......	IC 860	13 12 40.1	24 52 52	14.8	0.0131	
IR13254+4754......		13 25 25.7	47 54 38	16.0	0.0610	
IR13428+5608......	Mrk 273	13 42 51.6	56 08 14	15.0	0.0376	
IR13451+1232......		13 45 06.5	12 32 21	17.0	0.1213	2 nuclei observed
IR14566−1629......	N 5793	14 56 39.8	−16 29 56		0.0114	OH absorber
IR15065−1107......	N 5861	15 06 33.2	−11 07 56		0.0062	
IR15107+0724......	Zw 049.057	15 10 45.7	07 24 42	15.5	0.0128	
IR15179+3956......		15 17 55.8	39 56 23		0.0470	North component
IR15233+0533......		15 23 20.2	05 33 16		0.0541	
IR15247−0945......		15 24 43.6	−09 45 33	15.5	0.0395	
IR15250+3609......		15 25 03.2	36 09 02	15.5	0.0552	
IR15327+2340......	IC 4553, Arp 220	15 32 46.3	23 40 10	14.4	0.0180	2 nuclei observed
IR16399−0937......		16 39 55.2	−09 37 36	15.0	0.0269	2 nuclei observed
IR16577+5900......	N 6285	16 57 42.0	59 00 39		0.0184	OH absorber
IR17208−0014......		17 20 48.2	−00 14 17	15.0	0.0426	2 nuclei observed
IR17526+3253......	U 11035	17 52 39.1	32 53 36	14.3	0.0255	
IR18544−3718......		18 54 29.6	−37 18 41		0.073	Not observed
IR20100−4156......		20 10 05.8	−41 56 39	17.0	0.128	Not observed
IR20491+1846......	U 11643	20 49 08.1	18 46 57		0.0289	
IR20550+1656......	II Zw 96	20 55 05.3	16 56 03	15.2	0.0356	
IR22025+4205......	U 11898	22 02 31.9	42 05 05	15.7	0.0143	
IR22088−1832......		22 08 48.3	−18 32 07		0.170	Not observed
IR22491−1808......		22 49 09.5	−18 08 19	15.5	0.076	Sanders et al. (1988)
IR23050+0359......		23 05 01.3	03 59 33		0.0475	
IR23135+2516......	IC 5298	23 13 31.2	25 16 48	15.0	0.0272	
IR23365+3604......		23 36 31.5	36 04 26		0.0642	

NOTE—Units of right ascension are hours, minutes, and seconds, and units of declination are degrees, arcminutes, and arcseconds.

Figure B.1 Megamaser sources and general source properties.[45]

Figure B.2 Diagnostic diagram describing the separation of classifications between AGN, Starburst and composite sources.[45]The two lines indicates the dividing line between AGN, non-AGN and composite sources.

Index